J. Mech. Phys. Solids 191 (2024) 105774

Contents lists available at ScienceDirect

Journal of the Mechanics and Physics of Solids

journal homepage: www.elsevier.com/locate/jmps

Effects of nonlinearities and geometric imperfections on multistability and deformation localization in wrinkling films on planar substrates

Jan Zavodnik, Miha Brojan *

Faculty of Mechanical Engineering, University of Ljubljana, SI-1000 Ljubljana, Slovenia

ARTICLE INFO

Keywords:
Wrinkling
Multistability
Energy barrier
Imperfection
Nonlinear elasticity

ABSTRACT

Compressed elastic films on soft substrates release part of their strain energy by wrinkling, which represents a loss of symmetry, characterized by a pitchfork bifurcation. Its development is well understood at the onset of supercritical bifurcation, but not beyond, or in the case of subcritical bifurcation. This is mainly due to nonlinearities and the extreme imperfection sensitivity. In both types of bifurcations, the energy–displacement diagrams that can characterize an energy landscape are non-convex, which is notoriously difficult to determine numerically or experimentally, let alone analytically. To gain an elementary understanding of such potential energy landscapes, we take a thin beam theory suitable for analyzing large displacements under small strains and significantly reduce its complexity by reformulating it in terms of the tangent rotation angle. This enables a comprehensive analytical and numerical analysis of wrinkling elastic films on planar substrates, which are effective stiffening and/or softening due to either geometric or material nonlinearities. We also validate our findings experimentally. We explicitly show how effective stiffening nonlinear behavior (e.g., due to substrate or membrane deformations) leads to a supercritical post-bifurcation response, makes the energy landscape non-convex through energy barriers causing multistability, which is extremely problematic for numerical computation. Moreover, this type of nonlinearity promotes uni-modal, uniformly distributed, periodic deformation patterns. In contrast, nonlinear effective softening behavior leads to subcritical post-bifurcation behavior, similarly divides the energy landscape by energy barriers and conversely promotes localization of deformations. With our theoretical model we can thus explain an experimentally observed phenomenon that in structures with effective softening followed by an effective stiffening behavior, the symmetry is initially broken by localizing the deformation and later restored by forming periodic, distributed deformation patterns as the load is increased. Finally, we show that initial imperfections can significantly alter the local or global energy-minimizing deformation pattern and completely remove some energy barriers. We envision that this knowledge can be extrapolated and exploited to convexify extremely divergent energy landscapes of more sophisticated systems, such as wrinkling compressed films on curved substrates (e.g., on cylinders and spheres) and that it will enable elementary analysis and the development of specialized numerical tools.

* Corresponding author.
E-mail address: miha.brojan@fs.uni-lj.si (M. Brojan).

https://doi.org/10.1016/j.jmps.2024.105774
Received 22 April 2024; Received in revised form 30 June 2024; Accepted 7 July 2024
Available online 10 July 2024

1. Introduction

Wrinkling occurs when a thin structure adhered to a soft substrate is subjected to sufficiently large compressive membrane stresses either due to internal loads induced by temperature change, drying, residual stresses, or specific external loads. It can be undesirable, such as in drying fruit, skin aging, coating drying or in coating polymers with metals in transistor fabrication process (Liang et al., 2002), or desirable, e.g., for advanced functionalities such as wrinkled artificial skins (Huck, 2005), sound insulation (Hosseinpour et al., 2022), fabrication of smart surfaces enabling super-hydrophobic/hydrophilic behavior (Sabbah et al., 2016) and hydro-/aerodynamic drag reduction (Terwagne et al., 2014). Even mechanistic description of organ development can be attributed to wrinkling (Balbi et al., 2015; Ben Amar and Goriely, 2005).

The mechanics of wrinkling is a fairly well understood field, at least from the aspect of the linear bifurcation analysis (for a concise survey, see Nikravesh et al., 2020; Li et al., 2012). In the case of wrinkling with a super-critical pitchfork bifurcation, e.g., on some simple cases of beams and plates on an elastic foundation, the post-bifurcation regime can be explored with most commercial numerical modeling tools and simulated through mechanical compression, thermal expansion, growth, swelling, etc. The simplest but the most time-consuming way of numerical modeling is by using 3D solid finite elements (Li et al., 2011), which enables the use of an arbitrary material model. The computational cost can often be considerably reduced by using plate/shell kinematics to model the film without compromising much of the accuracy, see, e.g., Veldin et al. (2020, 2021). Ultimately, using the aforementioned kinematic assumptions on the film and modeling the effects of the substrate with the use of a Winkler type of substrate, the computational cost can be reduced even further, Veldin et al. (2020, 2019) and Stoop et al. (2015). This method produces results comparable to the experiments in terms of deformation. However, it can forecast critical loads that are up to 10 times larger than those observed experimentally.

In systems with a super-critical bifurcation wrinkling, such as wrinkling of films on linear (Huang et al., 2005) or stiffening substrates (Wang et al., 2023), a locally stable equilibrium solution in the immediate and moderate post-bifurcation regime can usually be obtained by following the continuous deformation evolution, which can be predicted by the linear bifurcation analysis in the post-bifurcation regime. However, as the magnitude of deformations increases further from the onset of wrinkling bifurcation, the potential energy landscape becomes increasingly more dependent on the (geometric and material) nonlinearities that promote non-convexity in the energy–displacement diagrams and therefore multiple locally stable equilibrium deformation states. If the original equilibrium path is stable (as it occurs in the case of a period-doubling bifurcation, see, e.g., Brau et al., 2011), other existing stable equilibrium paths may be difficult to observe, as they are divided by energy barriers in the energy landscape (for a concise summary of the concept see Hutchinson and Thompson, 2018). These energy barriers characterize the degree of local stability of each deformation state and are crucially important for the choice of a likely selected deformation state in a real system.

In contrast to the mechanics of wrinkling with super-critical bifurcation, where at least one of the equilibrium states can easily be found, it can be quite difficult to find any equilibrium state in the wrinkling of structures with sub-critical bifurcation. This category includes wrinkling in planar films on softening substrates (see, e.g., Hunt et al., 1989; Wadee et al., 1997; Thompson and Virgin, 1988) or wrinkling of cylindrical/spherical shells on elastic foundations (see, e.g., Brojan et al., 2015; Stoop et al., 2015; Veldin et al., 2019). Due to the material softening and eventual collapse of structural stiffness, the immediate post-bifurcation equilibrium path is extremely unstable. Immediately after the system reaches the bifurcation point, the structure experiences a wild dynamic jump from the trivial deformation state into a far-from-trivial equilibrium deformation state with much lower potential energy. Because this new stable equilibrium state is so far from trivial equilibrium, it has relatively large magnitudes of deformation with the choice of deformation patterns heavily governed by geometric/material nonlinearities. The deformation patterns are so-called spatial chaotic and analogous to those obtained in the time evolution of multidimensional nonlinear systems in chaos dynamic, see Hunt et al. (1989) and Lavrenčič et al. (2020). Because they are primarily governed by geometric/material nonlinearities, they are almost impossible to predict with linear bifurcation analysis. A typical example is the wrinkling of compressed cylinders, where a cylinder collapses to a far-from-trivial deformation state for which a multitude of possible deformation modes exists. The dynamic evolution of deformations together with geometric/material imperfections heavily impacts which locally stable energy minimum will be chosen, see Lavrenčič et al. (2020).

The first problem with analyzing the energy landscape of sub-critical bifurcation wrinkling, which is non-convex in an energy–displacement diagram, is the lack of robustness of the current numerical algorithms to find a stable equilibrium path as they quickly get lost in the multitude of unstable equilibrium paths right after the bifurcation point. In the case of super-critical bifurcation wrinkling, most of the algorithms are at least able to find a stable equilibrium but are oblivious to the co-existing locally stable branches as the standard path-following techniques (Veldin et al., 2021) only search locally. In contrast, dynamic algorithms are able to find different solutions but do not provide a direct way to select the solutions with the lowest potential energy or a systematic way to analyze the energy landscape, see Lavrenčič et al. (2020). Furthermore, numerical analysis requires discretization, which generally introduces imperfections that nonphysically alter the potential energy landscape.

Experimentally, analyses of post-bifurcation are even more difficult as geometric/material imperfections largely affect the energy landscape and promote certain modes while they suppress others. In the experiments, a virgin sample develops one of the locally stable deformation modes. The choice depends on the deformation path, loading rate, or initial imperfections; see Zavodnik et al. (2023). On the first try, the sample may plastically deform to some (rather small) extent, like in metal structures or in polymers, due to chain settling, etc. This filters out many other locally stable minima and deepens the energy valley of the chosen mode. Because of the changed energy landscape due to plasticity, the same original deformation mode develops after the unloading and reloading, regardless of the fact that the loading path and imperfections may be different this time.

Due to all these problems in numerical simulations and experiments, the existence of a multitude of simultaneous locally stable equilibrium solutions had only been found numerically by dynamic analysis of wrinkling in films on planar viscoelastic substrates, see Matoz-Fernandez et al. (2020) and Zavodnik et al. (2023). It was shown in these studies that during the deformation evolution, the rate of loading temporarily affects the potential energy landscape and can steer the deformations into different final locally stable states, divided by the energy barriers, of which the origin is not known yet — but is the focus of this study. The choice of the deformation state is, therefore, heavily affected by the whole evolution of the deformation pattern together with the perturbation forces and imperfections. The second problem with the analysis of such structures is that the stable equilibrium states differ in the "degree of stability". Therefore to be able to choose the equilibrium states with low potential energy and large surrounding energy barriers, which are likely to be chosen, the whole energy landscape has to be analyzed. Due to a large number of solutions and (geometric and/or material) nonlinearities, this is extremely hard and time-consuming when using brute-force numerical analysis. A systematic reduction of dimensionality of the analyzed system is therefore required to analyze the energy landscape globally and to find the locally stable equilibrium states, which are likely to be chosen by a system.

To tackle the mentioned challenges in the post-bifurcation analysis of wrinkling structures, we first focus on the analysis of a rather simple prototypical example: the wrinkling of an elastic film on a planar nonlinear elastic substrate. We set up an analytical and semi-analytical toy model based on Euler–Bernoulli beam assumptions and assuming finite displacements and finite rotations in modeling the film. This reduces the complexity of the problem and enables a systematic analysis of the post-bifurcation deformation patterns and the energy landscape. With the help of our theory, numerical simulations, and experiments, we analyze how different types of nonlinearities (symmetric/unsymmetric in tension and compression that come from either the film compressibility or the substrate nonlinearity) affect the energy landscape, determine whether the system has a sub- or super-critical post-bifurcation regime, and influence the most locally stable deformation patterns. Furthermore, we (1) explain why the post-bifurcation deformation patterns in the super-critical wrinkling are stable far into the post-bifurcation regime, (2) explain the multistability observed in Zavodnik et al. (2023), (3) explain the occurrence of different deformation patterns, which are unattainable by purely elastic systems, such as first observed in Matoz-Fernandez et al. (2020), (4) systematically analyze the energy barriers in-between locally stable states and how they are affected by initial imperfections, (5) explain the loss of periodic symmetry in sub-critical wrinkling, and (6) show/explain the loss and recovery of periodic pattern symmetry in experiments.

The rest of the paper is organized as follows: in Section 2, a beam theory reduced by incorporating Euler–Bernoulli beam assumptions is presented. In Section 3, the effects of nonlinearities on deformation patterns, such as period doubling, energy barrier due to nonlinearity, and deformation localization/periodicity, are presented. Moreover, the influence of initial imperfections on the energy landscape is analyzed using our theory, numerical simulations, and experiments. Relevance and the future outlook are discussed in Conclusions.

2. Theoretical formulation of the problem

We first derive a theory of deformations for *thin* beams under the Euler–Bernoulli assumptions that allow for the normal (bending and membrane) strains while neglecting the shear strains. Within these constraints, the theory is suitable for large displacement analysis of thin beams under small strain. To simulate the effects of the substrate to which the film (which we model as a beam) adheres, we prescribe effective normal and tangential external loads, which depend on the deformation of the film. The film is subjected to prescribed membrane strains due to growth or swelling.

2.1. Large displacement theory of an Euler–Bernoulli beam on a nonlinear substrate

The equilibrium equations for a thin beam in space are (see, e.g., Antman, 1973):

$$\begin{aligned} \boldsymbol{M}'(s) + (\boldsymbol{r}(s) \times \boldsymbol{F}(s))' + \boldsymbol{r}(s) \times \boldsymbol{f}(s) = 0, \\ \boldsymbol{F}'(s) + \boldsymbol{f}(s) = 0, \end{aligned} \tag{1}$$

where vector $\boldsymbol{M}$ is an internal moment, $\boldsymbol{F}$ is an internal force, $\boldsymbol{f}$ denotes the outer distributed forces, $\boldsymbol{r}$ denotes the position vector, while s, $s \in [0, l]$, denotes the natural (arc-length) parameter of the beam in the current configuration. The current length of the beam is denoted as l, while the reference length is denoted as $l_0 = l/\lambda$, with λ being the stretch due to growth, which is a load parameter in our case. The prime $(\ )' := d(\ )/ds$ denotes derivation with respect to s. By plugging Eq. $(1)_2$ into Eq. $(1)_1$, and differentiating, we obtain the following system of equations:

$$\begin{aligned} \boldsymbol{M}''(s) + \boldsymbol{t}'(s) \times \boldsymbol{F}(s) - \boldsymbol{t}(s) \times \boldsymbol{f}(s) = 0, \\ \boldsymbol{F}'(s) + \boldsymbol{f}(s) = 0, \end{aligned} \tag{2}$$

where $\boldsymbol{t}(s) = \boldsymbol{r}'(s)$ is a unit tangent vector. We adopt the Frenet–Serret frame with the tangent $\boldsymbol{t}(s)$, normal $\boldsymbol{n}(s)$ and a binormal $\boldsymbol{b}(s)$, where Frenet–Serret formulas narrate $\boldsymbol{t}'(s) = \kappa(s)\boldsymbol{n}(s)$, $\boldsymbol{n}'(s) = -\kappa(s)\boldsymbol{t}(s) + \tau(s)\boldsymbol{b}(s)$ and $\boldsymbol{b}'(s) = -\tau(s)\boldsymbol{n}(s)$. Here, κ is the curvature, and τ is the torsion of the space curve.

We consider a planar problem, which means that $\tau = 0$ and the binormal vector $\boldsymbol{b}$ is a constant unit out-of-plane vector. The internal moment, internal force, and the distributed external force can all be written in this frame as $(\boldsymbol{M}) = (0, 0, M)^{\mathrm{T}}$, $(\boldsymbol{F}) = (N, Q, 0)^{\mathrm{T}}$ and $(\boldsymbol{f}) = (f_t, f_n, 0)^{\mathrm{T}}$. Here, N is the normal section force, Q the tangential section force, and f_t and f_n the tangential and normal

components of the distributed outer forces that act on the beam, respectively. Due to the choice of the frame $(\boldsymbol{t}(s)) = (1,0,0)^{\mathrm{T}}$, $(\boldsymbol{n}(s)) = (0,1,0)^{\mathrm{T}}$ and both equations in Eqs. (2) can be rewritten as

$$M''(s) + N(s)\kappa(s) - f_n(s) = 0 \tag{3}$$

and

$$\begin{aligned} N'(s) - \kappa(s)T(s) + f_t(s) &= 0, \\ T'(s) + \kappa(s)N(s) + f_n(s) &= 0. \end{aligned} \tag{4}$$

In further derivations only Eq. $(4)_1$ will be used and the term $\kappa(s)T(s)$ will be neglected, as the product is rather small compared to $N'(s) + f_t(s)$ for moderately curved beams.

Now, according to the Euler–Bernoulli beam theory, the shear deformation is negligible, and therefore, the tangential section force can be calculated from Eq. $(4)_2$ and is not needed to calculate the deformation. Furthermore, according to the Euler–Bernoulli beam theory, the bending moment is proportional to the change of curvature. Without any curvature in the initial configuration, the bending moment is $M = -D\kappa$, where D is bending stiffness, more specifically $D = Eh^3/(12(1-\nu^2))$ in a plane strain case, where h, E and ν are the thickness of the beam, Young's modulus and Poisson's ratio, respectively, Lifshitz et al. (1986). Furthermore, the curvature can be expressed as the rate of change of the tangent vector, $\kappa = \varphi'(s)$. Finally, the equilibrium equations can be expressed in terms of the rotation of the tangent $\varphi(s)$ and the inner normal membrane force $N(s)$,

$$\begin{aligned} D\varphi'''(s) - N(s)\varphi'(s) + f_n(\varphi(s)) &= 0, \\ N'(s) + f_t(\varphi(s)) &= 0. \end{aligned} \tag{5}$$

We will consider cases of *nearly incompressible* and *incompressible* beam. Euler–Bernoulli type beams are usually considered incompressible, especially when they are subjected only to transverse loads because deformation modes other than bending can be neglected. In our case, the beam is primarily subjected to membrane forces that can cause some considerable membrane strains even if the membrane stiffness is relatively large compared to the bending stiffness due to the effect of the substrate. Therefore, in the case of a nearly incompressible beam, the relation between the membrane force $N(s)$ and the membrane strain of the beam can be modeled using a linear relation

$$N(s) = C(u'(s) + 1/\lambda - \cos\varphi(s)). \tag{6}$$

Here, $u(s)$ is the tangential displacement of the beam at s, $C = Eh/(1-\nu^2)$ is the membrane stiffness of the film, and $u'(s) + 1/\lambda - \cos\varphi(s) =: \varepsilon_{\mathrm{long}}$ is the longitudinal strain of the beam.

Comparing membrane and bending stiffnesses that $\sim h$ and $\sim h^3$, respectively, reveals that bending of thick beams severely penalizes the strain energy, which means that the membrane strains considerably increase its share in the total strain energy and that membrane strains are therefore not negligible. However, the substrate can suppress them considerably. For example, to obtain a certain number of wrinkles the substrate stiffness has to increase with increasing thickness. In thick beams this can go so far that the stiffness of the substrate becomes comparable to the membrane stiffness of the beam so that the substrate completely suppresses the tangential displacements of the beam, $u(s) = 0$. This leads to $N(s) = C(1/\lambda - \cos\varphi(s))$.

On the other hand, if the beam is thin, one can consider it *incompressible* and assume that the substrate shear tractions are negligible $f_t = 0$ compared to the membrane forces $N(s)$. Therefore, Eq. $(5)_2$ reduces to $N'(s) = 0$ and $N(s) = const. = -F$. From this, the tangential displacements can be evaluated as $u(s) = \int_0^s (\cos\varphi(s) - 1/\lambda)\, ds$ and since in a periodic deformation pattern $u(0) = 0$ and $u(l) = 0$, with l being the length of the film, we obtain the following incompressibility constraint,

$$\int_0^l \cos\varphi(s) ds - \frac{l}{\lambda} = 0. \tag{7}$$

For numerical calculations, it is easier to implement the compressible beam theory (which does not include any constraints) rather than the incompressible beam theory, in which the finite beam length requirement from Eq. (7) is given as a hard constraint in the strain energy optimization problem.

2.2. The role of the substrate in wrinkling

We consider the substrate to affect the beam as the normal stress f_n and the tangential stress f_t. In the case of the incompressible beam theory we neglect f_t, while in the case of the compressible beam theory we assume f_t is such that it prevents tangential film deformations $u(s) = 0$.

We further assume that the substrate is made of an incompressible (Hookean) material with a linear relation between stress and strain and that the deformation pattern is periodic. As shown by Allen (1969), Chen and Hutchinson (2004), Audoly and Boudaoud (2008) and Brau et al. (2011) expansion of the vertical displacement w into a Fourier series, $w(s) = \sum_{j=1}^{\infty} w_j \cos(k_j s)$, leads to the analytical solution for the normal traction $f_n(s) = 2\mu \sum_{j=1}^{\infty} k_j w_j \cos(k_j s)$. Using the small strain theory, where $\varphi(s) \approx w'(s)$, and Fourier series expansion of the rotation φ, $\varphi(s) = \sum_{j=1}^{\infty} \varphi_j \sin(k_j s)$, yields $\varphi(s) \approx -\sum_{j=1}^{\infty} w_j k_j \sin(k_j s)$. This means that $\varphi_j \approx -w_j k_j$. Using the known trigonometric identity $\cos(k_j s) = -i\sin(k_j s)$, where i is the imaginary unit, gives the normal traction with respect to φ_j, rather than to w_j, as $f_n(s) \approx 2\mu \sum_{j=1}^{\infty} \varphi_j i \sin(k_j s)$. Now, the expression for f_n can be written in terms of rotations as

$$f_n(s) \approx 2\mu i \varphi(s). \tag{8}$$

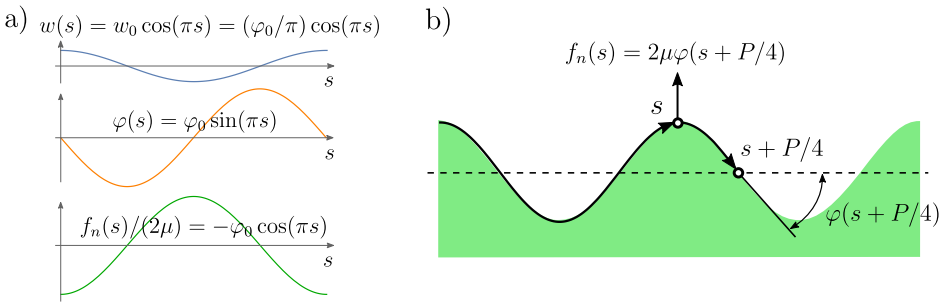

Fig. 1. Illustration of the phase shift between reaction force and rotation. (a) The normal reaction stresses $f_n(s)$ are proportional to rotation $\varphi(s)$, but in phase with vertical displacements $w(s)$. (b) For large deformations, the phase shift can be denoted by i; therefore, $f_n(s) \approx 2\mu\varphi(s + P/4) = 2\mu i\varphi(s)$.

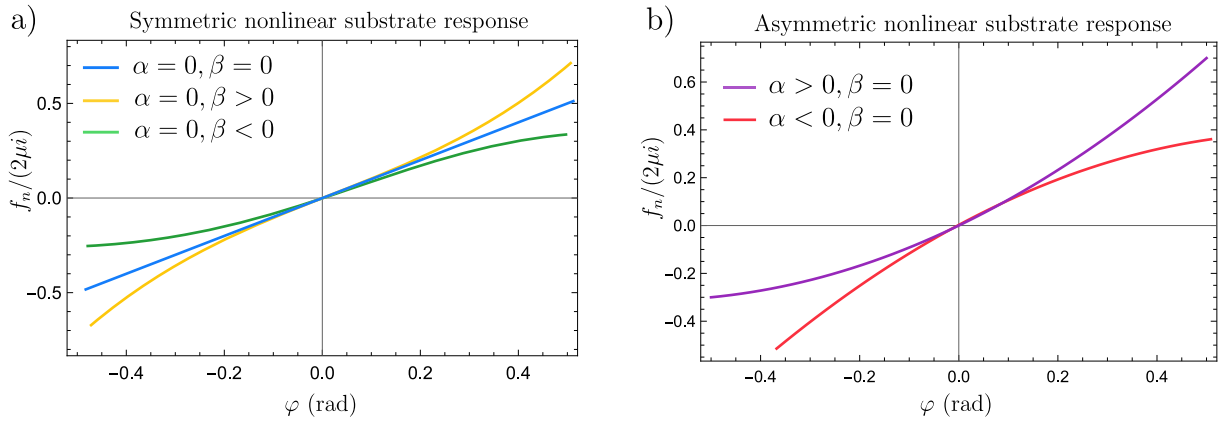

Fig. 2. Nonlinear response of a substrate. (a) Symmetric with stiffening ($\beta > 0$) or softening ($\beta < 0$). (b) Asymmetric with stiffening in tension and softening in compression ($\alpha > 0$, purple curve), and vice-versa ($\alpha < 0$, red curve). Coefficients α, β come from a truncated Taylor series expansion of the response of the substrate, see Eq. (9).

Note that the normal tractions depend on the magnitude of $\varphi(s)$ one quarter shifted, which means they are in phase with $w(s)$. This is denoted by multiplication with i, which can be summarized in $f_n(s) \approx 2\mu\varphi(s + P/4) = 2\mu i\varphi(s)$, where P is the period, and illustrated in Fig. 1(a) and (b).

Due to the slightly modified formulation of the beam theory presented above, the problem of wrinkling can be solved on the level of rotations $\varphi(s)$. Note that this way the relation between the traction forces and the rotation is linear and simpler than the classical description in terms of w_i given above. It also turns out to be more accurate within the proposed assumptions even though it is linear. This is because in the incompressible elasticity the connection between the rotation φ and the strains is significantly less nonlinear than the connection between vertical displacements w and the strains, see Fosdick and Schuler (1969).

In the following deliberations we do not differentiate between the geometrically, materially (or combined) caused stiffening or softening effects in terms of force-rotation. We will refer to these responses as *effective stiffening* or *effective softening*. The following cases will be studied:

1. Effective softening versus effective stiffening, as shown in Fig. 2(a) with a green and dark yellow curve, respectively, and
2. asymmetric versus symmetric response in tension and compression. In this paper, we only use an asymmetric response due to effective stiffening in one and effective softening in the other direction, as opposed to the asymmetric response that would arise due to different tangent stiffness for compression and for tension. The asymmetries we consider are displayed in Fig. 2(b) with red and purple, while symmetric nonlinearity is shown in Fig. 2(a) with green and dark yellow curves. The linear symmetric response is shown in blue.

In the next sections, we aim to explore how these different fundamental nonlinearity types cause the energy barriers between distinct deformation modes, the number of locally stable deformation states, the occurrence of periodic/localized deformation patterns, spatially-chaotic deformation patterns, and period doubling.

It was shown by Brau et al. (2011) that the substrate stress-deformation characteristic asymmetric in tension and compression causes period-doubling bifurcation, a secondary symmetry breaking of the pattern at large deformation. In their study, the nonlinear response of the substrate emanated purely from geometry (deformations) as it was based on a St. Venant-Kirchhoff material law, which describes the linear relationship between stress and strain states.

The period doubling, due to asymmetry in tension and compression, occurs only at relatively large loads of wrinkling systems. However, we will show that the nonlinear response that is symmetric in tension and compression, illustrated in Fig. 2(a), stabilizes/destabilizes the deformation pattern and causes its other qualitative changes much earlier, right at the onset of wrinkling. To capture the essential effects that follow from the nonlinearity, we will consider a substrate's response as a truncated Taylor series expansion

$$f_n(\varphi(s)) \approx 2\mu i(\varphi + \alpha(\varphi^2 - \langle\varphi^2\rangle) + \beta\varphi^3), \tag{9}$$

where parameter α, $\alpha \in \mathbb{R}$, characterizes the asymmetry in the nonlinear response in tension and compression, while β characterizes the effective stiffening and softening response when $\beta > 0$ and $\beta < 0$, respectively, see Fig. 2. The brackets $\langle\ \rangle := \int_0^l (\ )ds/l$ denote averaging along the beam — the idea results from the fact that the cumulative stress of the substrate has to be $\int_l f_n ds = 0$, meaning $\langle f_n\rangle = 0$.

Furthermore, we will show that the membrane strains of the beam cause symmetric nonlinearities in compression and tension and have a similar role to that of the substrate's symmetric nonlinearity due to effective stiffening. We will show that both of them determine the occurrence of either localized or a periodic uni-modal deformation pattern. We will also explain exactly how the symmetric nonlinearities cause energy barriers between the meta-stable deformation modes.

3. Results and discussion

We start our theoretical investigation at the onset of wrinkling. The case of super-critical bifurcation can be analyzed via a linear bifurcation analysis of Eq. $(5)_1$, which yields a classical result – a single uni-modal harmonic deformation mode in the deformation pattern. We assume that at the onset of wrinkling, the membrane force is constant $N(s) = -F$ and the reaction of the substrate is linear $f_n = 2\mu i\varphi(s)$. Solving the linear eigenvalue problem $D\varphi'''(s) + F\varphi'(s) - 2\mu i\varphi(s) = 0$, using a harmonic model function $\varphi(s) = \boldsymbol{\Phi}\exp(iks)$ yields a classical formula for the critical force $F = Dk^2 + 2\mu/k$, which depends on the eigenmode (wave number) $k = \pi n/l$, where n is the number of wrinkles. The structure acquires the lowest energy eigenmode that is permitted by the boundary conditions, which usually means that the number of wrinkles n must be an integer $k = \pi n/l$. This lowest energy eigenmode corresponds to the lowest non-trivial (nonzero) critical force F. In the case of an infinitely long structure, where the boundary conditions do not deny any eigenmodes, the lowest energy deformation mode is acquired by finding the mode with minimal membrane force using $dF/dk = 0$, from where

$$k_{\mathrm{cr}}^{\mathrm{inf}} = \sqrt[3]{\mu/D}, \tag{10}$$

while in the structures of finite length, the lowest energy eigenmode $k_{\mathrm{cr}}^{\mathrm{fin}}$, which has (half/)integer number of wrinkles, can be found close to $k_{\mathrm{cr}}^{\mathrm{inf}}$. With this at hand, the amplitude can be calculated from the incompressibility constraint given by Eq. (7). It is surprising that – at least for the case of super-critical wrinkling – even linear analysis gives rather good results for a system that undergoes moderately large deformations. In fact, as seen from the experiments by Brau et al. (2011) and simulations by Cao and Hutchinson (2012), a uni-modal deformation pattern globally minimizes the potential energy in the moderate range of deformations. As we will show next, this is the result of the stiffening nonlinearity in the system.

3.1. Nonlinear wrinkling analysis

In beam equilibrium in Eqs. (5), we assume that the normal component of the substrate traction is given in terms of a third-degree polynomial, see Eq. (9) and a membrane force in Eq. (6). We also approximate the quantities $\cos\varphi \approx 1 - \varphi^2/2$ and $1/\lambda \approx 1 - \varepsilon$, while truncating the higher order terms. We approximate the membrane strain of the film by $\varepsilon_{\mathrm{long}} \approx u'(s) - \varepsilon + \varphi^2/2$, where ε is a prescribed growth of the film, which is the load parameter in our theory. For the sake of simplicity, we will consider $f_t = 0$ in the incompressible beam case, as justified in Huang et al. (2005), or $u(s) = 0$, for the compressible beam case. Because we are mainly interested in qualitatively accurate results, we assume $\nu = 0.5$, although it was shown by Huang et al. (2005) that this will lead to an approximately 10% error. Considering all that, the approximated beam equilibrium equations are now

$$\begin{gathered} D\varphi'''(s) + C\left(u'(s) - \varepsilon + \frac{1}{2}\varphi^2\right)\varphi'(s) - 2\mu i(\varphi + \alpha(\varphi^2 - \langle\varphi^2\rangle) + \beta\varphi^3) = 0, \\ N'(s) = C\left(u'(s) - \varepsilon + \frac{1}{2}\varphi^2\right)' = 0. \end{gathered} \tag{11}$$

In the case of an incompressible beam both equilibrium equations apply, and the second can be solved as $N(s) = const. = -F$ and $u(s)$ can be integrated directly. The nonlinear system of ODEs can for instance be solved numerically, with the boundary conditions $\varphi(0) = \varphi(l) = \varphi''(0) = \varphi''(l) = 0$ and $N'(0) = N'(l) = -F$, where F is an unknown that can be calculated from the boundary conditions. The amplitude of the deformation pattern can be calculated from the incompressibility constraint or the membrane equilibrium. This way, the boundary value problem (BVP) is well posed and could be solved using, e.g., the shooting method.

In the compressible beam case, only the first equation from Eq. (11) applies, with $u(s) = 0$, while $N(s)$ can be calculated from Eq. (6).

We find that it advantageous to solve the BVP using the Fourier series as a model function (spectral method), which satisfies the boundary conditions naturally,

$$\varphi(s) = \sum_{i=1}^{\infty}\varphi_i(s) = \sum_{i=1}^{\infty}\boldsymbol{\Phi}_i\sin(k_i s). \tag{12}$$

Here, $k_i = \pi i/l$ are wave numbers, which are discrete values that satisfy the aforementioned boundary conditions, and Φ_i are the amplitudes of the deformation modes. This form of solution is especially well suited, when assuming no imperfections and a super-critical post-bifurcation. Only a single deformation mode is present at the onset of wrinkling, so it presents a way to make analytical predictions about the energy landscape.

To solve the system of ODEs in Eqs. (11), we first develop a potential energy functional for which this system is its first variation. Introducing function ϑ, $\vartheta(s) = \int \varphi(s)ds$, which is in the small strain theory the same as the vertical displacement w, integrating Eq. $(11)_1$ first with respect to $\delta\vartheta = \delta \int \varphi(s)ds$ and then along the length of the beam, yields the following potential

$$\Pi = \int_0^l \left(\frac{D}{2}\varphi'(s)^2 + \frac{C}{2}\left(u'(s) - \varepsilon + \frac{\varphi(s)^2}{2} \right)^2 + 2\mu i \int_0^{\vartheta} \left(\varphi + \alpha\left(\varphi^2 - \langle \varphi^2 \rangle \right) + \beta\varphi^3 \right) \delta\vartheta \right) ds. \tag{13}$$

In the case of incompressibility, the constant $C \to \infty$ leads to the condition in Eq. (7), which can be rewritten to $\int_0^l \left(\varepsilon - \varphi^2/2\right) ds = 0$ using Taylor series expansion. For the case of incompressibility ($N(s) = const. = -F$) the total energy can be replaced by

$$\Pi^{\text{incomp}} = \int_0^l \left(\frac{D}{2}\varphi'(s)^2 - F\left(-\varepsilon + \frac{\varphi(s)^2}{2} \right) + 2\mu i \int_0^{\vartheta} \left(\varphi + \alpha\left(\varphi^2 - \langle \varphi^2 \rangle \right) + \beta\varphi^3 \right) \delta\vartheta \right) ds, \tag{14}$$

where the term $\int_0^l F\left(-\varepsilon + \varphi(s)^2/2\right) ds$ is a Lagrange multiplier F multiplied by the incompressibility constraint. Using the fact that $\delta\vartheta = \delta \int \varphi(s)ds = -\sum_{i=1}^{\infty} \delta\Phi_i/k_i \cos(k_i s) = i\sum_{i=1}^{\infty} \delta\Phi_i(s)/k_i \sin(k_i s)$ (since $\cos(k_i s) = -i\sin(k_i s)$), we see that the total energy density per unit length in the incompressible case $\mathcal{E}^{\text{incomp}} = \Pi^{\text{incomp}}/l$ can be given as

$$\begin{aligned} \mathcal{E}^{\text{incomp}} = \sum_{i=1}^{\infty} \Bigg(& \frac{D}{4}k_i^2\Phi_i^2 - F\left(-\varepsilon + \frac{\Phi_i^2}{4} \right) + 2\mu \Bigg(\frac{1}{4}\frac{\Phi_i^2}{k_i} + \alpha \sum_{j=1}^{\infty}\sum_{k=1}^{j} \frac{C_{ij(k-j+1)(l-k+1)}}{k_i} \int_0^{\Phi_i} \Phi_j\Phi_{k-j+1}\delta\Phi_i \\ & + \beta \sum_{j=1}^{\infty}\sum_{k=1}^{j}\sum_{l=1}^{k} \frac{D_{ij(k-j+1)(l-k+1)}}{k_i} \int_0^{\Phi_i} \Phi_j\Phi_{k-j+1}\Phi_{l-k+1}\delta\Phi_i \Bigg) \Bigg). \end{aligned} \tag{15}$$

The harmonic correlation coefficients C_{ijk} and D_{ijkl} can be computed as $C_{ijk} = \int_0^l \sin(k_i s)\sin(k_j s)\sin(k_k s)ds/l$ and $D_{ijkl} = \int_0^l \sin(k_i s)\sin(k_j s)\sin(k_k s)\sin(k_l s)ds/l$.

In the case of a compressible beam, where we assume $u(s) = 0$, the total elastic strain energy density per unit length $\mathcal{E} = \Pi/l$ can be computed from (13) as

$$\begin{aligned} \mathcal{E} = \sum_{i=1}^{\infty} \Bigg(& \frac{D}{4}k_i^2\Phi_i^2 + \frac{C}{2}\left(\varepsilon^2 - \frac{\varepsilon\Phi_i^2}{2} + \frac{1}{4}\sum_{j=1}^{\infty}\sum_{k=1}^{j}\sum_{l=1}^{k} D_{ij(k-j+1)(l-k+1)} \int_0^{\Phi_i} \Phi_j\Phi_{k-j+1}\Phi_{l-k+1}\delta\Phi_i \right) \\ & + 2\mu \Bigg(\frac{1}{4}\frac{\Phi_i^2}{k_i} + \alpha \sum_{j=1}^{\infty}\sum_{k=1}^{j} \frac{C_{ij(k-j+1)(l-k+1)}}{k_i} \int_0^{\Phi_i} \Phi_j\Phi_{k-j+1}\delta\Phi_i \\ & + \beta \sum_{j=1}^{\infty}\sum_{k=1}^{j}\sum_{l=1}^{k} \frac{D_{ij(k-j+1)(l-k+1)}}{k_i} \int_0^{\Phi_i} \Phi_j\Phi_{k-j+1}\Phi_{l-k+1}\delta\Phi_i \Bigg) \Bigg). \end{aligned} \tag{16}$$

Variation of Eqs. (16) and (15) with respect to Φ_i yields a so-called spectral method approximation, which will later be used to solve our system in Section 3.4. Nonetheless, we first use the total energy density in Eq. (16) to qualitatively analyze the energy landscape with respect to Φ_i.

3.2. Period doubling due to quadratic-type substrate nonlinearity

To validate our theory, we first analyze the already well-researched topic of period-doubling bifurcation in wrinkling. To reiterate, this phenomenon is the result of an asymmetric stress response of the substrate in tension and compression (see Fig. 2(a)). In the work of Brau et al. (2011), the St. Venant-Kirchhoff material model was used, which describes a linear relationship between stress and strain and employs Green–Lagrange strain tensor, which leads to a quadratic nonlinear theory that is asymmetric because it exhibits stiffening in tension and softening in compression.

Since the deformation patterns found at the immediate and moderate post-bifurcation response are similar, Brau et al. (2011), and the immediate post-bifurcation can be obtained from the linearized analysis of Eq. (15) or (16), i.e. as a harmonic solution $\varphi(s) = \sum_{i=1}^{\infty} \Phi_i \sin(k_i s)$, we also use it in the moderate post-bifurcation at this point. We take two deformation modes $k_n = k$ and $k_{2n} = 2k$ and use the nonlinear theory only for assessing the stability of the solution. Here, $2k = (\mu/D)^{1/3}$ is the wavenumber of the deformation mode that minimizes the strain energy at the onset of wrinkling for an infinitely long beam. We redefine the amplitudes $\Phi_n = -A$ and $\Phi_{2n} = -B$, while keeping $\beta = 0$ for the sake of simplicity. Similarly, we can assume for the incompressible beam that $C \to \infty$, which then assures that $\int_0^l \left(\varepsilon - \varphi^2/2\right) ds = 0$ or equivalently $4\varepsilon = A^2 + B^2$. With these assumptions, we obtain the total strain energy density of the incompressible beam given in Eq. (15) for the two deformation modes

$$\mathcal{E} = \frac{D}{2}\left(\frac{A^2k^2}{2} + \frac{4B^2k^2}{2} \right) + \frac{2\mu}{k}\left(\frac{1}{2}\left(\frac{A^2}{2} + \frac{B^2}{4} \right) - \frac{\alpha}{4}A^2B \right). \tag{17}$$

Note that the energy consists of quadratic bending and substrate energy contributions due to linear material laws and also a cubic contribution $-\alpha A^2 B/4$, which comes from the quadratic nonlinearity of the substrate. At the onset of wrinkling, the primary

deformation mode with the wavenumber $2k$ has the amplitude $B = \sqrt{4\varepsilon}$ due to the incompressibility constraint, while the secondary mode is not present, i.e., $A = 0$, since its increase would increase the bending and linear part of substrate energy more than it would decrease the nonlinear substrate energy through $-\alpha A^2 B/4$. However, if the load ε exceeds a secondary bifurcation strain $\varepsilon_{2\text{nd}} = (32\alpha/5)^{-2}$ the Hessian determinant of the Lagrangian $\mathcal{E}^{\text{incomp}}$ becomes negative, which suggests a period-doubling saddle point bifurcation. This result coincides with the results of Brau et al. (2011). Our theory suggests that after $\varepsilon > (32\alpha/5)^{-2}$ the increase in amplitude A decreases the energy due to the nonlinear part of the substrate energy $-\alpha A^2 B/4$ more than it increases the linear bending and substrate energies. Therefore, it is energetically more favorable to have a combination of the deformation modes k and $2k$ with amplitudes A and B, rather than to have a single deformation mode.

More intuitively, the substrate softens with compression and strengthens with tension. Therefore, rather than equally tensioning one half and compressing the other half of the surface of the substrate, as is the case with uni-modal deformation pattern, it is energetically more efficient to only mildly tension a large area and to intensely compress a small area to likewise achieve an equilibrium, but at minimal strain energy. This is achieved exactly by the composition of the modes with $2k$ and k wavenumbers, which manifests a period doubling in the physical space.

3.3. Energy barrier due to cubic-type nonlinearity

The period-doubling bifurcation causes large qualitative changes in deformation patterns only at the relatively late post-bifurcation stage, at large loads ε. In contrast, the nonlinearity symmetric in tension and compression that we are about to explore only causes drastic qualitative changes if it is softening. However, both, the effective stiffening and the effective softening symmetric nonlinearities (see Fig. 2) critically affect the strain energy landscape because they stabilize or destabilize the uni-modal deformation patterns, respectively.

To obtain a basic insight into the energy landscape, we again first analyze some simple deformation patterns, which are the solutions of the linear version of Eqs. (5) with $f_t = 0$, while we use the nonlinear Eq. (16) to analyze stability. We assume the solution is composed of a mixture of only two consecutive deformation modes: (i) $k_n = k = \pi n/l$ and (ii) $k_{n-1} = g = \pi(n-1)/l$, where the number of half-waves n are integers, as allowed by the boundary conditions. We denote their amplitudes (real numbers due to the boundary conditions) as $\Phi_n = A$ and $\Phi_{n-1} = B$. Considering this, the averaged total strain energy density in Eq. (16) over a large domain $l \to \infty$ yields

$$\begin{aligned}\mathcal{E} = &\frac{D}{2}\left(\frac{A^2k^2}{2} + \frac{B^2g^2}{2}\right) + \frac{C}{2}\left(-\frac{\varepsilon}{2}\left(A^2+B^2\right) + \frac{3}{32}\left(A^4 + 4A^2B^2 + B^4\right)\right)\\ &+ 2\mu\left(\frac{1}{2}\left(\frac{A^2}{2k} + \frac{B^2}{2g}\right) + \frac{3\beta}{32}\left(\frac{A^4}{k} + \frac{2A^2B^2}{k} + \frac{2A^2B^2}{g} + \frac{B^4}{g}\right)\right).\end{aligned} \tag{18}$$

This strain energy density form is central to our analysis of all the following phenomena and will be referred to throughout the rest of the paper. Its arguments, i.e., amplitudes of the two modes A, B and their wavenumbers k and g, have to be chosen to minimize the form. We can divide the strain energy form into well-known classical linear contributions (quadratic in terms of amplitudes A and B in strain energy) that govern the choice of deformation pattern wavenumber at the onset of wrinkling (but surprisingly also later on) and its nonlinear contributions (quartic functions of the amplitudes A and B in terms of energy), which govern the stability of deformation patterns, and are at the heart of our investigation.

To minimize the classical linear terms, which govern the onset of wrinkling, the amplitudes of the modes (A and B) have to be such that they optimize the total strain energy. Because the membrane stiffness coefficient C is much larger than the bending and substrate coefficients D and μ, respectively, the amplitudes of the modes must primarily minimize the membrane strain energy. Furthermore, because the membrane strain energy is so dominant, the amplitudes are often calculated directly from the beam incompressibility constraint $\int_0^l \left(\varepsilon - \varphi^2/2\right) ds = 0$ or equivalently $4\varepsilon = A^2 + B^2$. This constraint gives the magnitude of wrinkling, while the minimization of bending and (linear) substrate strain energy provides the share of the wrinkle magnitude each mode will take. All modes release membrane energy from the system through $-\varepsilon\left(A^2+B^2\right)/2$, however at the expense of additional bending energy $D/4\left(A^2k^2 + B^2g^2\right)$ that penalizes large wavenumbers and substrate strain energy $\mu\left(A^2/k + B^2/g\right)/2$ that penalizes small wavenumbers. The optimal mode $k_{\text{opt}}^{n\in\mathbb{R}} = \sqrt[3]{\mu/D}$ is, therefore, a compromise for releasing as much membrane energy as possible while not raising neither too much bending, nor too much strain energy of the substrate. Without the integer restriction on the number of half waves n the deformation pattern is uni-modal with $k_{\text{opt}}^{n\in\mathbb{R}} = \sqrt[3]{\mu/D}$ and the amplitude of angle φ is $\sqrt{4\varepsilon}$. If n is an integer, then the optimal wavenumber is $k_{\text{opt}}^{n\in\mathbb{N}} = \pi n_{\text{opt}}^{\text{int}}/l$, which can be found near $\sqrt[3]{\mu/D}$ and the amplitude of the angle φ is still $\sqrt{4\varepsilon}$.

In our nonlinear analysis, we first assume the optimal wavelength and magnitudes of wrinkles are the same as in the linear case and use the nonlinear terms to analyze the stability of these solutions and the energy barriers between them. Therefore, we choose our first mode to have the optimal wavenumber in view of the linear analysis with $k = k_{n+1} = k_{\text{opt}}^{n\in\mathbb{N}} = \pi n_{\text{opt}}/l$ with integer n_{opt}. This optimal wavenumber $k = k_{\text{opt}}^{n\in\mathbb{N}}$ can be found close to $\sqrt[3]{\mu/D}$. Then we choose our second mode to also obey the boundary condition's integer constraint on n and to be a neighbor of the optimal one n_{opt} but with one less half-wave $g = k_{n-1} = \pi(n_{\text{opt}} - 1)/l$. Provided n_{opt}/l is much larger than one, k and g are almost the same, $k \approx g$. This greatly simplifies the explanation of further analysis. Furthermore, we observe that although our strain energy in Eq. (16) includes asymmetric quadratic nonlinearity (cubic functions of A and B in terms of strain energy) with coefficient α, it has vanished in Eq. (18) due to considering only two consecutive deformation modes and energy density averaging. Therefore, we can focus on the terms from the symmetric cubic nonlinearity (quartic terms of

A and B) that remain. They arise due to (i) the membrane strain energy of the beam in $3C\left(A^4+4A^2B^2+B^4\right)/64$ and (ii) due to effective stiffening/softening of the substrate with $6\mu\beta\left(A^4/k+2A^2B^2/k+2A^2B^2/g+B^4/g\right)/32$, see Section 2.2 and Fig. 2(a).

With this in at hand, we can finally analyze the stability of the structure with the energy form given in Eq. (18), where the symmetric nonlinearities of both sources provide pure quartic terms A^4 and B^4, but most importantly they provide mixed terms A^2B^2, which are the source of all of the phenomena we are covering. Provided the substrate is effective softening with sufficiently small β (when $\beta<0$), such that the negative term βA^2B^2 of the substrate dominates over the positive terms A^2B^2 of the membrane strains, then the mixed deformation patterns (with both $A\neq 0$ and $B\neq 0$) have a lower strain energy than purely uni-modal deformation patterns. Therefore, in general, softening promotes mixed, multi-modal deformation patterns in the modal space, which is expressed as the localization of deformation in the physical space. This will be further explored in Section 3.4.

In contrast, provided $\beta>0$ or when the term A^2B^2 dominates over the negative term of the substrate βA^2B^2, mixed deformation states (with $A\neq 0$ and $B\neq 0$) are penalized compared to the uni-modal deformation patterns. This suggests that a nonlinear deformation stiffening system, either due to membrane strains or effective stiffening substrate, promotes uni-modal deformation patterns even in a moderate or large deformation regime. This has also been seen but not explored more in depth in experiments and simulations in Brau et al. (2011) and Chen and Hutchinson (2004).

More importantly, positive terms A^2B^2 provide an energy barrier between uni-modal deformation patterns. This is because the transition of the structure from one uni-modal state to another demands passing through higher energy mixed-modal states, where the energy is higher due to A^2B^2. The reason, that going through mixed states is necessary, is either due to beam incompressibility constraint $A^2+B^2=4\varepsilon$, or due to the fact that in a compressible beam the membrane stiffness C is usually large and even a small deviation from $A^2+B^2-4\varepsilon=0$ leads to a large increase in energy. Therefore, going through a mixed state with additional A^2B^2 is energetically more efficient, but still requires additional energy input to increase the energy during the transition. This is all true provided that $g\approx k$ so that the change from one sub-optimal state (e.g., $A=0$, $B=\sqrt{4\varepsilon}$) to globally optimal state (e.g., $A=\sqrt{4\varepsilon}$, $B=0$) does not lower the linear bending and substrate energies so much, that they override the increase of energy due to the mixed A^2B^2 terms.

For a more concrete mathematical description of the described energy barrier, consider an incompressible beam with $C\to\infty$ with the incompressibility constraint $A^2+B^2=4\varepsilon$. With that, the energy functional in Eq. (18) loses a mixed energy term A^2B^2 due to membrane strain energy. However, because the effective stiffening (i.e., $\beta>0$) provides the same effect, no generality is lost, while the energy barrier is easier to show. We assume that a deformation pattern under the incompressibility constraint with a constant prescribed membrane strain load ε, evolves from a sub-optimal uni-modal deformation mode ($A=0$, $B=\sqrt{4\varepsilon}$, $g=\pi(n_{\text{opt}}-1)/l$) to an optimal uni-modal deformation mode ($A=\sqrt{4\varepsilon}$, $B=0$, $k=\pi n_{\text{opt}}/l$). For an easier display of the evolution we introduce parametrization $A=\sqrt{4\varepsilon}\sin\Theta$ and $B=\sqrt{4\varepsilon}\cos\Theta$, which automatically satisfies the beam incompressibility constraint $4\varepsilon=A^2+B^2$. Furthermore, since the load ε is fixed, only one parameter $\Theta=\arctan(A/B)$, which represents the share of each of the two consecutive single deformation modes' amplitudes, describes the evolution. For example at $\Theta=0\Rightarrow B=\sqrt{4\varepsilon}$ and $A=0$ and at $\Theta=\pi/2\Rightarrow B=0$ and $A=\sqrt{4\varepsilon}$. Introducing this change of variables to the total strain energy density in Eq. (18), yields bending and substrate terms only, which are functions of the constant ε and the share parameter Θ:

$$\begin{aligned}\mathcal{E}(\Theta)=&D\varepsilon\left(g^2\cos^2\Theta+k^2\sin^2\Theta\right)+2\mu\varepsilon\left(\frac{\cos^2\Theta}{g}+\frac{\sin^2\Theta}{k}\right)\\&+6\beta\varepsilon^2\mu\left(\frac{\cos^4\Theta}{2g}+\frac{\cos^2\Theta\sin^2\Theta}{g}+\frac{\cos^2\Theta\sin^2\Theta}{k}+\frac{\sin^4\Theta}{2k}\right).\end{aligned}\tag{19}$$

In Fig. 3, the strain energy density $\mathcal{E}$ of uni-modal deformation modes with an integer number of half-waves n is depicted by dots. Between the integer values of n, we plot the strain energy (given by Eq. (19)) of the deformation pattern, which is composed of a mixture of the consecutive integer modes, parameterized by Θ.

Inset (i) shows a close-up of the transition from the case with 6 half-waves to 7 half-waves in the effective stiffening case. Effective stiffening ($\beta>0$) – or equivalently membrane strain energy in thicker beams – causes an energy barrier between both uni-modal deformation modes and, therefore, creates a multistable system with many locally stable deformation modes. This explains why in the wrinkling of elastic film on visco-hyperelastic halfspace (Zavodnik et al., 2023) and in the wrinkling of viscoelastic plates (Matoz-Fernandez et al., 2020) multiple final deformation states (unobtainable by the purely elastic deformations) were found. Due to the energy barriers resulting from the aforementioned nonlinearities, these states might be local energy minima or states close to one, which makes the evolution toward the lower (local) minimum extremely slow. This was the case in Zavodnik et al. (2023) where both the compressibility of the film and the standard viscoelastic neo-Hookean substrate provided energy barriers and, therefore, multistability, together with the observation of an extremely slow evolution from meta-stable to globally stable deformation patterns. Inset (ii) in Fig. 3 shows that a linear substrate and the incompressible film exhibit no energy barrier between single deformation modes. Finally, inset (iii) shows that in systems with softening substrates, a deformation pattern composed of many deformation modes is energy minimizing, and uni-modal deformation patterns are not stable. Ultimately, the composition of multiple deformation modes in the modal space means localization of deformation in the physical space. In general, softening behavior can also come from geometric nonlinearity, such as in the buckling of spherical shells, where the deformation localizes (Hutchinson, 2016; Paulose and Nelson, 2012; Vliegenthart and Gompper, 2011).

(**The effect of initial imperfections on the energy barrier**) The energy barrier due to a effective stiffening substrate or membrane strains in the film can be largely affected by the initial imperfections or perturbation forces acting on the structure. To show this, we assume that the structure is already winkled before deformation with initial wrinkles with the amplitude B_0 and sub-optimal wavenumber $g=\pi(n_{\text{opt}}-1)/l$. We define a relative difference between the length of the film and its projection, which

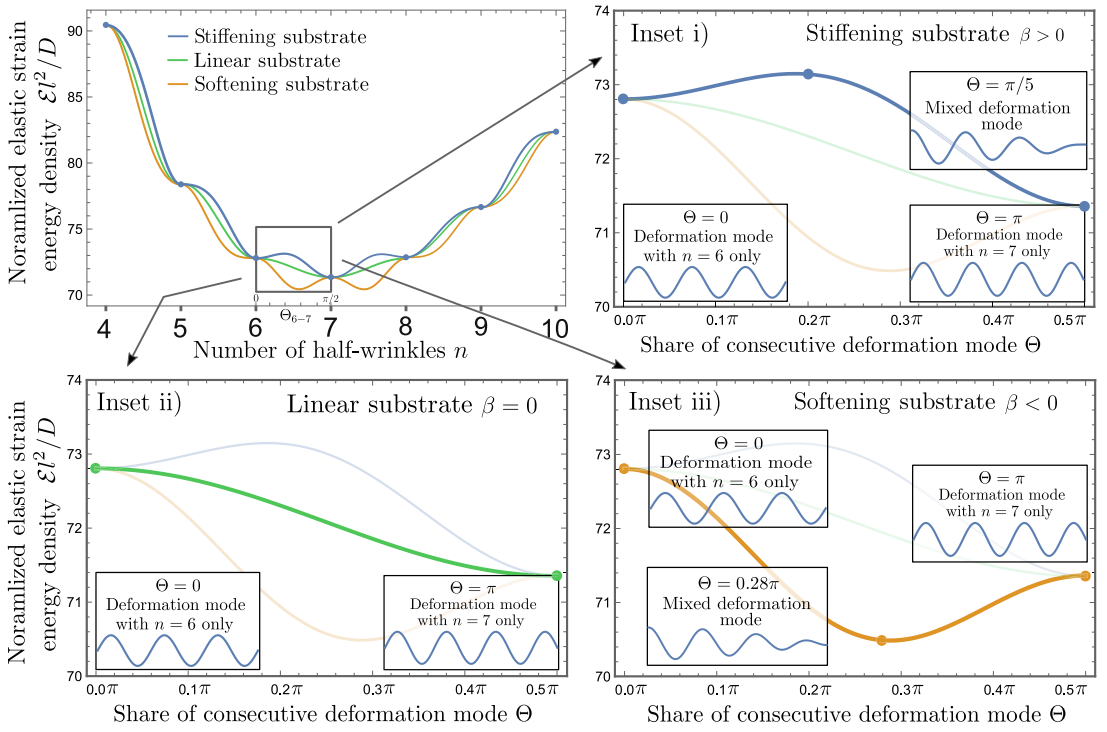

Fig. 3. Elastic strain energy density landscape of finite length beam on a planar elastic substrate as a function of integer number of half-wave n, which is due to boundary conditions. In between the integer values n, we assume that deformation patterns are a composition of consecutive n and $n+1$ deformation modes. This composition is parameterized by $\Theta = \arctan A/B$, the share parameters between consecutive mode's amplitudes A and B. Blue curves represent a effective stiffening substrate with $\beta = 0.5$, green curves a linear substrate with $\beta = 0$ is linear, and orange curves a softening substrate with $\beta = -0.5$. Here, with the ratio $2\mu l^2/D = 20\,000$, the energetically optimal n is $n_{\mathrm{cr}}^{\mathrm{int}} = 7$, considering the integer constraint of n due to boundary conditions, while without the boundary condition constraint $n_{\mathrm{cr}}^{\mathrm{real}} = 6.858$. Zoom-in views of the segment represent the strain energy density: (i) Of a composition of uni-modal deformation modes $n = 6$ and $n = 7$ for effective stiffening substrate $\beta = 0.5$. The three sub-insets in this insert show the deformation patterns of an isolated (uni-modal) $n = 6$, $n = 7$ mode, and a composed deformation mode. To evolve from the locally stable $n = 6$ deformation mode into the globally energetically favorable $n = 7$ deformation mode, the deformation pattern has to become a composition of both modes due to the constraint $4\varepsilon = A^2 + B^2$ and, therefore, pass through the energy barrier due to energy terms due to nonlinear contribution A^2B^2 which penalizes composed modes. (ii) In the case with a linear substrate with $\beta = 0$, no energy barriers prevent the transition from uni-mode with $n = 6$ to a uni-mode with $n = 7$ half-waves. (iii) Finally, in the case of softening substrate with $\beta = -0.5$, uni-modal deformation states are unstable, and the energetically favorable deformation pattern is composed of both consecutive uni-modes.

can be calculated as $\varepsilon_0 = B_0^2/4$. In the strain energy of the system given in Eq. (18) we replace the membrane strain energy with a Lagrange multiplier and a beam incompressibility condition $\varepsilon = (A^2 + (B + B_0)^2)/4 - B_0^2/4$ to obtain a system, which is equivalent to Eq. (14) with two modes only. And since $\varepsilon_0 = B_0^2/4$ we obtain

$$\begin{aligned}\mathcal{L} = {} & \frac{D}{2}\left(\frac{A^2k^2}{2} + \frac{B^2g^2}{2}\right) + F\left((\varepsilon + \varepsilon_0) - \frac{A^2 + (B + B_0)^2}{4}\right) \\ & + 2\mu\left(\frac{1}{2}\left(\frac{A^2}{2k} + \frac{B^2}{2g}\right) + \frac{3\beta}{32}\left(\frac{A^4}{k} + \frac{2A^2B^2}{k} + \frac{2A^2B^2}{g} + \frac{B^4}{g}\right)\right),\end{aligned} \tag{20}$$

Without initial imperfections B_0, the system of equations that we obtain by searching for a minimum of the Lagrangian above would be homogeneous, and F would be unknown, but now, due to imperfection, F is a load parameter. If we again apply $A = \sqrt{4\varepsilon}\sin\Theta$ and $B = \sqrt{4\varepsilon}\cos\Theta$, we obtain the following Lagrangian function

$$\begin{aligned}\mathcal{L} = {} & D\varepsilon\left(k^2\sin^2\Theta + g^2\cos^2\Theta\right) + 2\mu\varepsilon\left(\frac{\sin^2\Theta}{k} + \frac{\cos^2\Theta}{g}\right) \\ & + 6\beta\varepsilon^2\mu\left(\frac{\sin^4\Theta}{2k} + \frac{\cos^2\Theta\sin^2\Theta}{k} + \frac{\cos^2\Theta\sin^2\Theta}{g} + \frac{\cos^4\Theta}{2g}\right) \\ & - FB_0\sqrt{4\varepsilon}\cos\Theta.\end{aligned} \tag{21}$$

The last term $-FB_0\sqrt{4\varepsilon}\cos\Theta$ makes the system of equations non-homogeneous and decreases the total strain energy of the structure, especially of the same deformation mode, i.e., the same wavenumber g as the imperfection. Note that the load parameter F can be calculated from ε only in equilibrium, where $\partial\mathcal{L}/\partial\Theta = 0$ holds, and therefore, we parameterize the imperfection with FB_0 and not with B_0 alone.

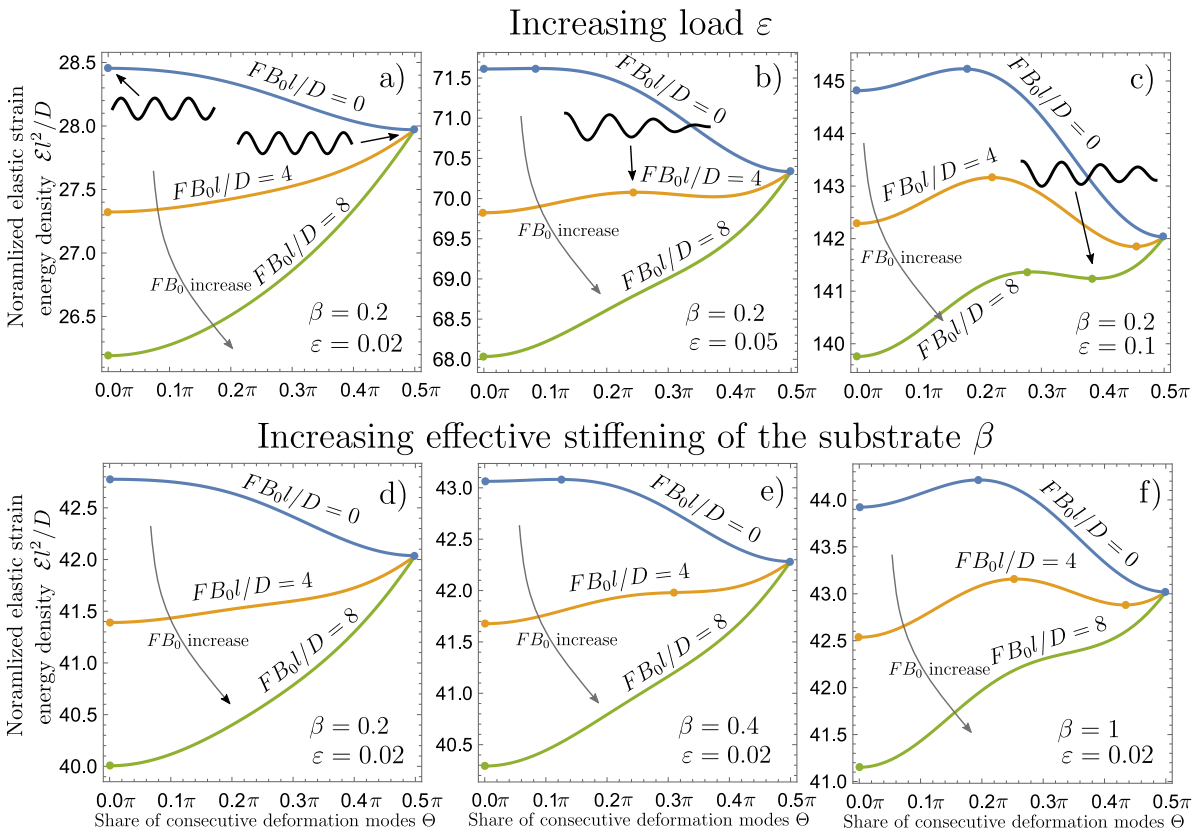

Fig. 4. Normalized strain energy $\mathcal{E}l^2/D$ from Eq. (21) as a function of parameter Θ, which determines the share two modes (in this particular case of geometric and material parameters either $n=6$ or $n=7$). When $\Theta=0$ the pattern is uni-modal with $n=6$, when $\Theta=\pi/2$ the pattern is uni-modal with $n=7$, while Θ in-between, the pattern is composed of both modes. First row shows that the increase in the prescribed membrane strain ε, $\varepsilon\in\{0.02,0.05,0.1\}$, increases the energy barrier between the two modes, while at the same time the increase in parameter FB_0 (B_0 measures the amplitude of the initial geometric imperfection) decreases it or removes it completely (green curve in panel (b)). Similarly, the second row shows that the increase in effective stiffening coefficient β, $\beta\in\{0.2,0.4,1\}$, increases energy barrier between the two modes, while parameter FB_0 decreases it or removes it completely (green curves in panels (e) and (f)).

Fig. 4 shows the strain energy calculated from Eq. (21) in relation to the share parameter Θ describing the involvement of the two modes with wavenumbers $k=7\pi/l$ and $g=6\pi/l$. This means if $\Theta=0$ or equivalently $B=\sqrt{4\varepsilon+B_0^2}-B_0$ this corresponds to a uni-axial state $n=6$, while if $\Theta=0.5\pi$ or equivalently $A=\sqrt{4\varepsilon}$ this corresponds to the uniaxial state $n=7$. Panel (a) in Fig. 4 shows the one dimensional energy landscape in terms of the strain energy as a function of Θ. One can observe from the first row, panels (a)–(c), that the increase in the prescribed membrane strain ε, $\varepsilon\in\{0.02,0.05,0.1\}$, increases the energy barrier between the two modes, while at the same time the increase in parameter FB_0 (B_0 measures the amplitude of the initial geometric imperfection) decreases it or removes it completely (green curve in panel (b)). Similarly, the second row shows that the increase in effective stiffening coefficient β, $\beta\in\{0.2,0.4,1\}$, increases energy barrier between the two modes, while parameter FB_0 decreases it or removes it completely (green curves in panels (e) and (f)).

(**Deformation pattern composed from multiple modes**) Until now, only deformation patterns consisting of two deformation modes were considered to simplify the explanations. We will show that similar arguments can be extended to a case of multiple modes. For the sake of simplicity, let us assume that the deformation pattern consists of only deformation modes of similar wrinkle wavenumbers $k_i\approx k$. Then using the incompressibility constraint of the film $4\varepsilon=\sum_{i=1}^{\infty}\Phi_i^2$, the total energy density in Eq. (16) can be rewritten in terms of the load ε as

$$\mathcal{E}\approx D\varepsilon k^2+2\mu\frac{\varepsilon}{k}+2\mu\frac{3\beta}{2k}\left(\varepsilon^2+e_{ijkl}\sum_{\substack{i,j,k,l=1\\ i\neq l,j\neq k}}^{\infty}\Phi_i\Phi_j\Phi_k\Phi_l\right). \tag{22}$$

Terms that depend only on load strain ε are independent of how the deformation is shared between the modes' amplitudes Φ_i, and therefore, they do not penalize or promote the deformation states composed of multiple modes. In contrast, terms $\Phi_i\Phi_j\Phi_k\Phi_l$ with

coefficients e_{ijkl}, which are all positive (not explicitly given for brevity), provide the energy barrier/valley depending on the sign of β. These terms are analogous to $\beta A^2 B^2$ terms in Eq. (18) and with $\beta > 0$ penalize or with $\beta < 0$ promote mixed deformation modes.

Therefore, in general, uni-modal deformation patterns noticed in experiments in wrinkling of films on substrates, e.g., in our experiments presented later in Fig. 5(a) or Brau et al. (2011), most likely originate from effective stiffening substrate and are stabilized by the energy barriers. Conversely, multi-modal deformation patterns, which manifest as localization of deformation in physical space, are probably caused by some sort of softening effect, e.g., as in our experiments shown in Fig. 5(b).

3.4. Uni-modal periodic vs. localized deformation pattern

To analyze how effective stiffening/softening in the substrate affects the distribution of deformation across the surface, we employ our theory, numerical simulations, and experimental methods. In the potential energy density functional, Eq. (16), we vary the amplitudes of the deformation modes to find fixed points, equivalent to static equilibriums with

$$\begin{aligned}\delta\mathcal{E}(\boldsymbol{\Phi}_i,\delta\boldsymbol{\Phi}_i) = \sum_{i=1}^{\infty}\Bigg(&\frac{D}{2}k_i^2\boldsymbol{\Phi}_i + C\left(\frac{1}{2}\sum_{j=1}^{\infty}\sum_{k=1}^{j}\sum_{l=1}^{k} D_{ij(k-j+1)(l-k+1)}\boldsymbol{\Phi}_j\boldsymbol{\Phi}_{k-j+1}\boldsymbol{\Phi}_{l-k+1} - \frac{\varepsilon}{2}\boldsymbol{\Phi}_i\right)\\ &+2\mu\Bigg(\frac{1}{2}\frac{\boldsymbol{\Phi}_i}{k_i} + \alpha\sum_{j=1}^{\infty}\sum_{k=1}^{j}\frac{C_{ij(k-j+1)(l-k+1)}}{k_i}\boldsymbol{\Phi}_j\boldsymbol{\Phi}_{k-j+1}\delta\boldsymbol{\Phi}_i\\ &+\beta\sum_{j=1}^{\infty}\sum_{k=1}^{j}\sum_{l=1}^{k}\frac{D_{ij(k-j+1)(l-k+1)}}{k_i}\boldsymbol{\Phi}_j\boldsymbol{\Phi}_{k-j+1}\boldsymbol{\Phi}_{l-k+1}\Bigg)\Bigg)\delta\boldsymbol{\Phi}_i = 0.\end{aligned} \tag{23}$$

For finding the combination of modes that constitute equilibrium, we first choose a sufficient range of modes $k_i = \pi i/l$, $i \in \{1, 2, \dots, 20\}$, which satisfy the boundary conditions. In order to solve the nonlinear system of equations for $\boldsymbol{\Phi}_i$, we add an artificial viscous part to the equation in the form $\tau\dot{\boldsymbol{\Phi}}_i\delta\boldsymbol{\Phi}_i = -\delta\mathcal{E}(\boldsymbol{\Phi}_i,\delta\boldsymbol{\Phi}_i)$, where $\dot{(\,)} = d(\,)/dt$ and τ is an artificial viscoelastic constant (we chose 1), so that the system converges. The initial conditions are set to $\boldsymbol{\Phi}_i(t=0) = 10^{-2}$.

We performed numerical analysis using our theory and Abaqus on three samples to show that effective stiffening with $\beta > 0$ induces periodic deformation patterns and a super-critical bifurcation (see Fig. A.8(a) in Appendix A.3), while effective softening with $\beta < 0$ induces localized wrinkling and a super-critical bifurcation (see Fig. A.8(b)–(c) in Appendix A.3). On two samples with thin film the nonlinear effects of only the substrate are analyzed, while on the third sample with a thick film the combined effects of the substrate nonlinearity and the membrane effects are analyzed. In all cases we keep $\alpha = 0$ to explore the effects of β only. We compared the numerical results to the experimental results at 4 wavelengths of the sample, i.e. $n_{\mathrm{cr}} = 8$. The wavelength of wrinkles predicted by the theory matched that from the experiments. Both, the experiments and simulations were displacement controlled such that the amplitudes of the deformation patterns qualitatively matched the experimentally obtained ones. Note that such comparison is valid because this problem is mainly governed by the geometric effects due to film incompressibility.

(*i*) *A thin film on an effective stiffening substrate*

Fig. 5(a) and (c) show the results of the numerical analyses of a compressed thin film on an effective stiffening substrate, using our theory and Abaqus, respectively. Geometric and material properties were taken from the experiment presented in Fig. 5(b). They were as follows: the film of length $l = 26$ mm and the thickness $h = 0.47$ mm with Young's modulus $E_{\mathrm{f}} = 5.2$ MPa was fixed onto a rubber substrate with tangential Young's modulus $E_{\mathrm{s}} = 0.165$ MPa. A similar experiment was conducted by e.g. Brau et al. (2011). According to the linearized wrinkling analysis using Eq. (10) $k_{\mathrm{cr}} = 8\pi/l$ or equivalently $\lambda_{\mathrm{theor.}} = 6.47$ mm, is obtained, which matches the experimentally measured wavelength $\lambda_{\mathrm{exp.}} = 6.36$ mm quite well. In Abaqus, a neo-Hookean material model was used for modeling the substrate. A rectangular block of a neo-Hookean substrate that is loaded multiaxially provides an effective stiffening effect on the film (note that a neo-Hookean material exhibits effective strain softening in a uni-axial extension, see Fig. A.9 in Appendix A.4). Because there exist no finite strain analytical solutions for the response of the substrate, we are unable to calculate the coefficient of the nonlinearity β exactly. Therefore we choose $\beta = 0.5$ study an effective stiffening response. This results in a periodic uni-modal deformation pattern, as explained in Section 3.3. As pointed out in Zavodnik et al. (2023), many of these local energy-minimizing uni-modal deformation patterns can occur, depending on the deformation evolution, which is governed by the initial conditions, load rate, and viscoelastic properties of the structure, but also by initial imperfections, as explained in the previous subsection. More on the numerical simulations and experiments can be found in the Appendix.

Even though imperfections imposed in the simulation might be localized before deformation, the final deformation pattern is periodically symmetric, as suggested by our analysis in Section 3.3, where we point out that mixed modes are penalized in effective stiffening structures. Intuitively explained, this is because the compressed film releases some membrane energy through some amount of wrinkling (bending) while it gains a smaller amount of energy in bending and substrate deformation. Intuitively, in an effective stiffening substrate, it is easier to strain more of the un-strained substrate than to additionally strain the already strained substrate. Therefore, if the mentioned amount of wrinkling is as uniformly distributed as possible (uni-modal deformation mode), it raises the total energy of the substrate less than if the same amount of wrinkling is localized. In an effective stiffening structure, uni-modal deformation modes are forms of the most uniformly distribute deformation and are, therefore, preferred in effective stiffening structures.

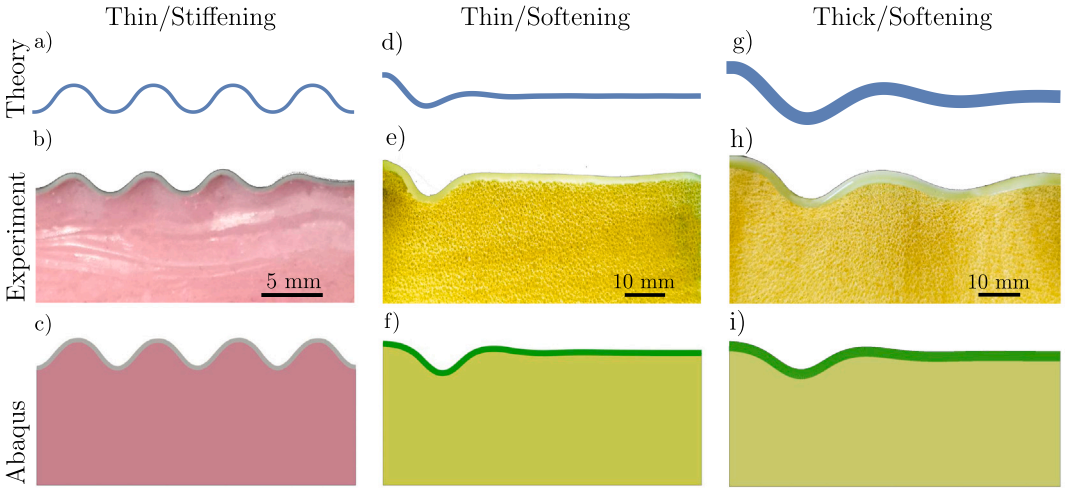

Fig. 5. Deformation patterns from our theory, experiments and simulations. The results are given for thin film with an effective stiffening substrate (a)–(c) and softening substrate (d)–(f), while for a thick film on a softening substrate was assumed to obtain images in panels (g)–(i). Young's moduli of the film E_f were 5.2, 1.3 and 1.3 MPa, tangential Young's moduli of the substrate were $E_{s,tang.}$ 0.165, 0.0380 and 0.0380 MPa, and thicknesses of the film h were 0.47, 1.55 and 2.65 mm, respectively. The observed wavelengths of the patterns on the experimental samples were $\lambda_{exp.}$ 6.36, ≈23, ≈40 mm, while the theoretical predictions for the wavelength $\lambda_{theor.}$ from the linearized theory yielded 6.47, 21.9, 37.4 mm, respectively. (a) Theoretical prediction of a stable single mode deformation pattern due to effective stiffening of the substrate. Here, the deformation shape is calculated from $x(s) = \int \cos\varphi(s)ds$ and $y(s) = \int \sin\varphi(s)ds$. (b) Result of a desktop experiment with a stiffer film (gray) and a softer substrate (pink). The details of the experiment are given in the Appendix. (c) Simulation results obtained with Abaqus using a neo-Hookean substrate. The parameters used are described in the Appendix. (d) Our theory predicts a localization of deformations in the substrate made from foam, which exhibits strong softening. (e) Our desktop experiment with green rubber and blackboard sponge as a substrate. (f) Our simulations in Abaqus where the substrate is modeled as a hyperfoam, which is described in the Appendix. (g) Our theory predicts a reduction in the localization of deformation due to a thicker film, which stabilizes deformation. (h) An experiment with a blackboard sponge and a thicker rubber substrate, which causes deformation delocalization. (i) A simulation with hyperfoam as a substrate and a thicker elastic substrate in Abaqus.

(*ii*) *A thin film on an effective softening substrate*

Fig. 5(e) shows a localized deformation pattern, obtained experimentally through the compression of a film on a sponge that exhibits an effective softening response. Again, very similar patterns were obtained in simulations, see Fig. 5(d) and (f). The sample had a film with length $l = 80$ mm, thickness $h = 1.55$ mm and the Young's modulus $E_f = 1.3$ MPa was fixed onto a substrate with a Young's modulus $E_s = 0.0380$ MPa. The theoretical wavelength is $\lambda_{theor.} = 21.9$ mm, while experimentally $\lambda_{exp.} = 23$ mm was measured. To simulate the response of the sponge we used the hyperfoam material model in Abaqus. Again, because there exist no analytical solution for a finite strain hyperfoam substrate response, we chose $\beta = -0.85$, which exhibits effective softening response and deformation localization. The location of localization is usually the location of the largest imperfection or perturbation load, where the material is already deformed. Therefore, further deformation of the substrate is easier than deforming a virgin material. This is also visualized in Fig. 3(d), where the strain energy landscape analysis suggests that deformation patterns are composed of multiple modes, which translate to localization of deformation in the physical space, as also suggested by our analysis in previous sections.

Similar deformation localization phenomena due to softening substrates were theoretically observed in Wadee et al. (1997) and Hunt et al. (1989) but have not yet been reproduced experimentally. To the best of our knowledge our wrinkling experiments on effective softening substrates were done for the first time.

(*iii*) *A thick film and a softening substrate*

Fig. 5(h) shows another (somewhat) localized deformation pattern on an experimental sample on a thicker film with thickness $h = 2.65$ mm. Similar deformation patterns were obtained with the use of our own theoretical model and Abaqus, see Fig. 5(g) and (i), respectively. Here the classical linearized wrinkling theory yields $\lambda_{theor.} = 37.4$ mm, which is comparable to the experimentally observed wavelength $\lambda_{exp.} \approx 40$ mm. Here, due to a thicker substrate the sample regains the periodic symmetry to some extent already at the beginning. This happens due to the interplay between the effective softening of the substrate and membrane strains in the film that have a similar effect as an effective stiffening substrate. As apparent form samples (*i*) and (*ii*), the effective softening substrate promotes the localization of deformation, whereas the effective stiffening substrate penalizes the localization of deformation. The latter is significantly emphasized in thick films because the thickness increases the bending rigidity, $D \sim h^3$, and with that, the normal membrane force required for the loss of stability quickly becomes large. This results in large membrane strains, due to a disproportionately smaller increase in membrane rigidity, $C \sim h$.

3.5. Discussion on the loss and recovery of the symmetry

In all experiments with effective stiffening and softening substrates, we observed that by continuously applying a compressive load to a film adhered to an elastic substrate, the first symmetry breaking and wrinkle development occur at the location of an

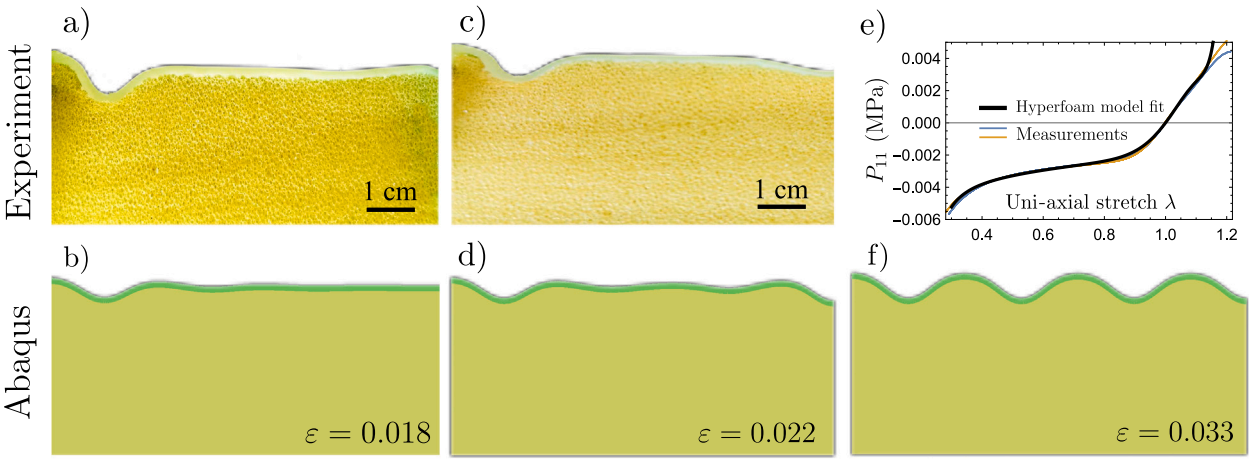

Fig. 6. (a–b) Localization of deformation observed close to the onset of wrinkling in experiments due to a softening characteristic of the substrate at prescribed strain of the film in experiments and simulations (at $\varepsilon = 0.018$), respectively. (c–d) Reorganization and recovery of periodic symmetry due to effective stiffening behavior of the more deformed portions of material in experiments and simulations (at $\varepsilon = 0.022$), respectively. (e) The measured and fit first Piola–Kirchhoff stress tensor component P_{11} vs. uniaxial stretch λ for a uniaxial stress–strain characteristic of the hyperfoam substrate used in the simulations. (e) Recovery of the symmetric deformation pattern that contains a singular deformation mode at $\varepsilon = 0.033$. Experimentally, we were not able to obtain such a deformation pattern due to large asymmetry in the compressive vs. tensile response of the foam, which caused large period doubling behavior. The material parameters for the hyperfoam material model, which were obtained by fitting our uniaxial experimental stress–strain curves, are given as $\mu_1 = 0.2$, $\mu_2 = 0.1270$, $\mu_3 = 0.00196$, $\mu_4 = -0.00032$, $\mu_5 = 8.4 \times 10^{-6}$, $\alpha_1 = 20$, $\alpha_2 = 21$, $\alpha_3 = 37$, $\alpha_4 = -0.5$, $\alpha_5 = -4$ and $\beta_1 = \beta_2 = \beta_3 = \beta_4 = \beta_5 = 0$. Such material behavior matches that in the study of Attenburrow et al. (1989). More on the methods in simulations and experiments is given in the Appendix.

imperfection. This happens because an imperfection or perpendicular forces (usually at the edge) all locally deform the structure, providing a lever to the compressive forces in the film to produce a bending moment and form wrinkles there. However, upon increasing the load in structures with effective stiffening substrates or thick films, the deformation pattern soon de-localizes as mixed (localized) deformation modes become increasingly penalized by the nonlinear effects, which gain in significance with deformation magnitude, as presented in the previous Section 3.3. On the contrary, in structures with a softening substrate and a thin film, the deformation localization is further promoted by the substrate. Such a case is seen in our example in experiments and simulations in Fig. 6(a)–(b).

To analyze the loss and recovery of symmetry in our experimental and numerical examples in Fig. 6(a)–(f) we used a moderately thick film and a foam material, which indeed first experiences a softening behavior but later undergoes a rapid effective stiffening (a uni-axial stress–strain curve is given in Fig. 6(e)). Because of this, the deformation pattern localizes at the left edge as seen in Fig. 6(a)–(b) for a relatively small load ($\varepsilon = 0.018$), while upon its increase, the effective stiffening in the material and the effects of a thick substrate take over and cause the deformation pattern to spread across the entire sample rising a periodic symmetry. With further increase in the load to $\varepsilon = 0.033$ the sample in numerical simulations completely recovers its periodic symmetry as shown in Fig. 6(f). Note that we were not able to achieve this with our particular experimental sample. We attribute this to the large asymmetric response in tension and compression. For further details on the simulations and experiments, see Appendix.

4. Conclusions

In this study, we analyzed wrinkling in films on planar substrates and discussed how the substrate nonlinearities and imperfections affect multistability, degree of stability, and deformation localization due to the non-convex potential energy landscape. We have shown that we can largely reduce the dimensionality of the solution through the large displacement theory based on rotations, helping us circumvent the numerical problems associated with the large amount of available solutions (multistability) in the analysis of the energy landscape.

Our theoretical model includes nonlinear contributions from the membrane strain energy of the beam (geometric nonlinearities) and the deformation of the substrate (material nonlinearities). This enables us to access the mechanism of how the membrane energy in the film and/or effective softening/stiffening of the substrate causes numerous locally stable deformation modes (multistability) and affect the degree of their stability by controlling the size of the energy barriers between them. Moreover, we find that they also dictate whether the deformation is localized or distributed across the structure. Specifically, we show that the effective stiffening effects cause super-critical post-bifurcation behavior and support multiple periodically symmetric deformation patterns that are distributed across the structure, and their corresponding local minima are divided by the energy barriers. In contrast, the effective softening (e.g., in foams) causes sub-critical post-bifurcation behavior and supports localized deformations with the corresponding local energy minima that also divided by the energy barriers. Therefore, such structures experience a dynamic jump to far-from-trivial equilibrium deformation states with relatively large localization of deformation patterns. The localization due to softening is permanent, as opposed to that induced by viscoelastic effects, see Zavodnik et al. (2023) and Audoly (2011).

Our theory also helps us analyze the effect of initial imperfections and initial conditions in the evolving structure and can directly explain why some numerically found deformation modes can be found in experiments while others cannot, such as in Zavodnik et al. (2023) and Matoz-Fernandez et al. (2020). With our theory, we also recover the results from Brau et al. (2011) in the analysis of period-doubling bifurcation. Finally, we observed that in materials with softening, followed by the effective stiffening behavior, the first loss of stability has a sub-critical post-bifurcation response, which means a discontinuous jump from a (non-stable) periodic pattern to a localized deformation pattern. This is then followed by a recovery of periodic symmetry with an increase in the load.

Although we analyzed wrinkling in thin films on nonlinear planar substrates, we anticipate that similar arguments can be extended to wrinkling in thin films on 3D planar and curved substrates, such as in wrinkling of films on a half-space, cylinder, sphere, torus, etc. We anticipate that analogous to our theory and experiments, the Gaussian curvature in an initially curved structure might supply an additional geometric rigidity and also a localized softening behavior after the symmetry breaking, which potentially transforms to stiffening behavior, which recovers the symmetry in the pattern. In fact, the loss and recovery of periodic symmetry with deformation magnitude were observed, e.g., in wrinkling in films on spherical (Brojan et al., 2015; Veldin et al., 2019), and cylindrical substrates (Lavrenčič et al., 2020) experimentally and numerically. On curved shells, we additionally anticipate the energy barriers due to stiffening/softening nonlinearities divide the energy landscape into numerous local energy minima with similar potential energies, which makes such problems notoriously difficult to solve even numerically.

Although convexification methods are already used in optimization (McCormick, 1976; Tuy and Van Thuong, 1988; Tawarmalani and Sahinidis, 2002), they are based on empirical/heuristic arguments. Usually, the energy landscape has to be computed first in order to be convexified, which is extremely computationally expensive in cases with large number of degrees of freedom, such as in wrinkling of thin films on elastic substrates. For wrinkling films on effective stiffening/softening planar substrates, we have extracted the influencing parameters, i.e., source terms, that control the energy barriers and multistability. We anticipate that this is possible also on structures with initial curvature (shells). These parameters still have to be identified and adjusted to convexify the energy with respect to the sought displacements before computing.

CRediT authorship contribution statement

Jan Zavodnik: Writing – original draft, Software, Methodology, Investigation, Formal analysis, Conceptualization. **Miha Brojan:** Writing – review & editing, Supervision, Resources, Project administration, Methodology, Investigation, Funding acquisition, Conceptualization.

Declaration of competing interest

The authors declare that there are no conflict of interest regarding the publication of the paper. The manuscript is original and has not been published or considered to be published in other journals.

Data availability

Data will be made available on request.

Acknowledgment

The authors gratefully acknowledge the financial support of the Slovenian Research Agency, Slovenia (project grant numbers J2-9223 and J2-2499).

Appendix. The experiment and numerical simulations

A.1. Experiments

Our experiments shown in Figs. 5 and 6 were made with rubber material, which exhibits effective stiffening, and a foam material, which exhibits an effective softening response. A film made from either gray (QSil 550 A) with $E = 5.2$ MPa or green (Elite double 32) rubber with $E = 1.3$ MPa was placed onto either a pink (Elite Double 8) rubber material with $E = 0.165$ MPa or a yellow blackboard sponge made from polyurethane foam with tangential Young's modulus $E = 0.0380$ MPa. All the tangential moduli were measured using a compressive test, except for the foam, which was also extended.

In the experiment in Fig. 5(b), a softer (pink Elite Double 8) rubber was poured on a film made of a stiffer (gray QSil 550 A) rubber material, which was polymerized beforehand. The softer rubber then shrunk during curing which induced initial wrinkling that was even further increased by additionally squeezing of the sample. Similarly, in the softening experiments in Fig. 5(e), (h) and Fig. 6(a) and (c) an already polymerized rubber material (green Elite Double 32) was fixed to a polyurethane foam cut from a blackboard sponge (yellow) using an additional fresh mix of green rubber, which acted as glue. The structure was then compressed using a clamp, thereby ensuring fixed boundary conditions.

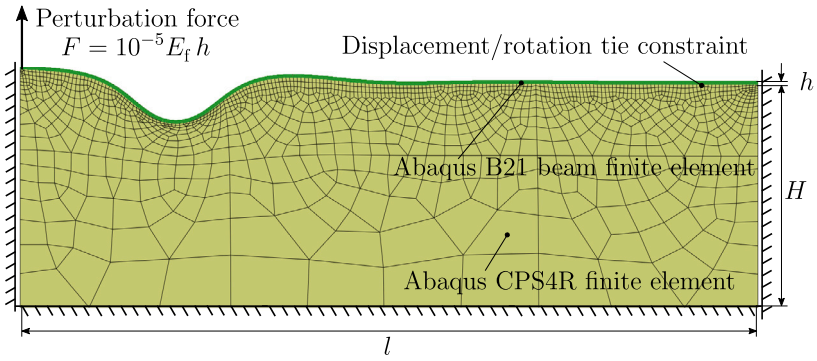

Fig. A.7. The domain for numerical simulations. The displacement and rotational degrees of freedom of a beam were tied to those of the underlying 2D solid.

A.2. Abaqus simulations

We used a neo-Hookean and Hyperfoam material model for the substrate made from silicon rubber and foam, respectively. A beam B21 Abaqus finite element was used and tied to a 2D solid (CPS4R Abaqus element); see Fig. A.7. At both vertical edges, the horizontal displacement was fixed, while the vertical was free. All displacements were fixed at the bottom. The normal compressive membrane stresses that induced wrinkling were imposed through heating of the beam with a thermal expansion coefficient $\alpha = 1$.

The tangential stiffness of the rectangular incompressible neo-Hookean substrate is 2μ, which can be obtained from the incompressibility assumption, see e.g. Audoly and Boudaoud (2008). The wavenumber $k = \pi n/l$ at the onset of wrinkling, therefore, depends on the ratio $k = \sqrt[3]{\mu/D}$, and does not significantly change with the growing magnitude of wrinkles.

Unless special algorithms for bifurcation analyses are implemented, numerical solvers, such as commercial ones, require a perturbation to find a non-trivial, wrinkled solution. In our case, we initiated wrinkling with a small vertical perturbation force at the edge of the domain (see Fig. A.7) of the magnitude $F = 10^{-5} Eh$, which produces a negligible influence on the deformation field. Such a type of perturbation also agrees with experimental results, where wrinkling usually starts at the edge due to experimental imperfections at the boundary.

To be able to simulate wrinkling in both cases of the sub- and super-critical post-bifurcation case, a static Riks path following algorithm was used. To obtain the solutions presented in Figs. 5 and 6, the combinations of parameters (such as perturbation force magnitude, path step, and expected path length) had to be determined by trial and error.

Two different material models were used; a *neo-Hookean* and a *Hyperfoam* material to simulate a stiffening and a softening substrate, respectively.

(Thin film on a stiffening substrate) In the simulation with a stiffening material in Section 3.4, displayed in Fig. 5(c), the film was modeled with standard beam elements with the beam thickness $h = 0.47$ mm, length of $l = 26$ mm and Young's modulus $E = 5.2$ MPa in Abaqus, while a neo-Hookean material model was used for the substrate. Its elastic strain energy density can be written as $W = \mu\,(\mathrm{tr}(\mathbf{C}) - 2)/2 + \lambda(\det(\mathbf{C}) - 1)^2/2$, Smith (2009) where $\mathbf{C}$ is the right Cauchy–Green deformation tensor and μ and λ are the shear modulus and first Lame parameter, respectively. To simulate incompressible behavior, we used a material constant λ, much larger than $\mu = E/3$, where $E = 0.165$ MPa. Such material exhibits effective stiffening in wrinkling, although it is effective softening in uni-axial extension.

(Thin film on a softening substrate) In the simulation in Section 3.4, displayed in Fig. 5(f), the film was also modeled using standard beam elements with the beam thickness $h = 1.55$ mm, length of $l = 80$ mm and Young's modulus $E = 1.3$ MPa in Abaqus. Here, the substrate was modeled using a hyperfoam material. Such hyperfoam material has a strain energy given by Ogden strain energy density function $W = \sum_{i=1}^{5} \mu_i/\alpha_i^2 \left((\lambda_1^{\alpha_i} + \lambda_2^{\alpha_i} + \lambda_3^{\alpha_i} - 3) + ((\lambda_1\lambda_2\lambda_3)^{\alpha_i\beta_i} - 1)/\beta_i\right)$, see, e.g., Smith (2009) where λ_j are the principle stretches. For the sake of simplicity, we neglected the volumetric part, as we assumed that there is no Poisson effect. We measured the uniaxial stress–strain curve of the foam material, which we fit with the coefficients in the Ogden hyperfoam material model with $\mu_1 = 0.2$, $\mu_2 = 0.1270$, $\mu_3 = 0.00196$, $\mu_4 = -0.00032$, $\mu_5 = 8.4 \times 10^{-6}$, $\alpha_1 = 20$, $\alpha_2 = 21$, $\alpha_3 = 37$, $\alpha_4 = -0.5$, $\alpha_5 = -4$ and $\beta_1 = \beta_2 = \beta_3 = \beta_4 = \beta_5 = 0$. The uni-axial stress–strain experimental results and the fit are shown in Fig. 6(e). It clearly shows softening behavior in smaller strain regimes that becomes stiffening at larger stretches.

(Relatively thick film on a softening substrate and reorganization of deformation pattern) In Section 3.4 Fig. 5(i) and Section 3.5 Fig. 6(b), (d) and (f) the substrate was modeled using a hyperfoam material as in the previous case, while the film was thicker with $h = 2.65$ mm with the same other geometric and material properties as before.

A.3. Nature of bifurcations

Fig. A.8(a) shows that a thin film on an effective strain stiffening substrate exhibits a super-critical bifurcation when compressed. On the other hand, Fig. A.8(b) and (c) show that an effective softening substrate exhibit a sub-critical bifurcation. In these two cases the post-bifurcation response is multistable and therefore much more difficult to analyze numerically. When numerically analyzing such systems with the softening response, even the advanced path-following algorithms may encounter serious difficulties (see a recent paper on the solution Kusuma Chandrashekhara and Zupan, 2024).

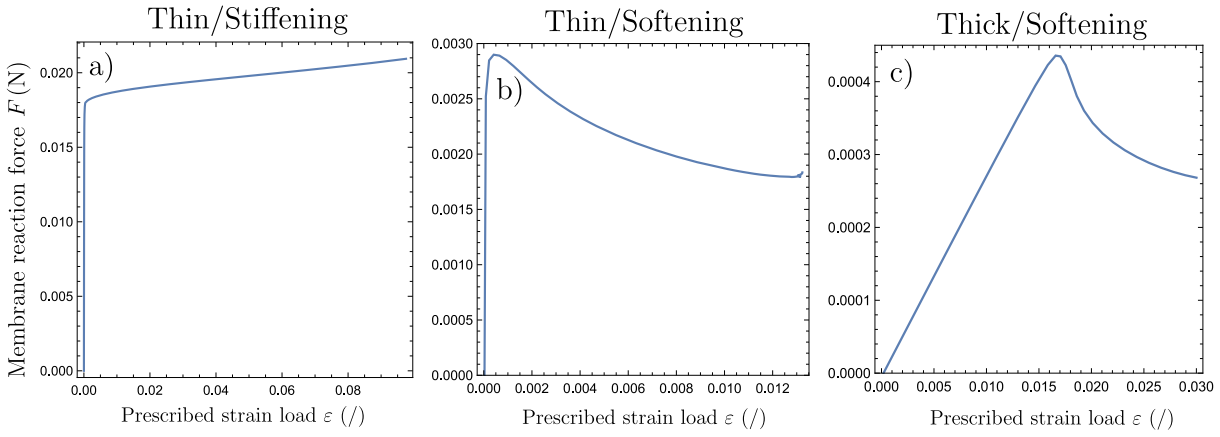

Fig. A.8. The diagrams (a)–(c) show the membrane reaction force at the left boundary F of the film as a function of the load strain ε. The diagrams (a), (b) and (c) correspond to the deformation patterns from the simulations in Fig. 5(a), (d) and (e) respectively. The panel (a) shows wrinkling film on a neo-Hookean substrate, which due to its effective strain stiffening has a super-critical bifurcation. Conversely, panels (b) and (c) show a thin and a thick wrinkling film on a Hyperfoam material, respectively. The Hyperfoam material is effective strain softening and therefore has a sub-critical bifurcation.

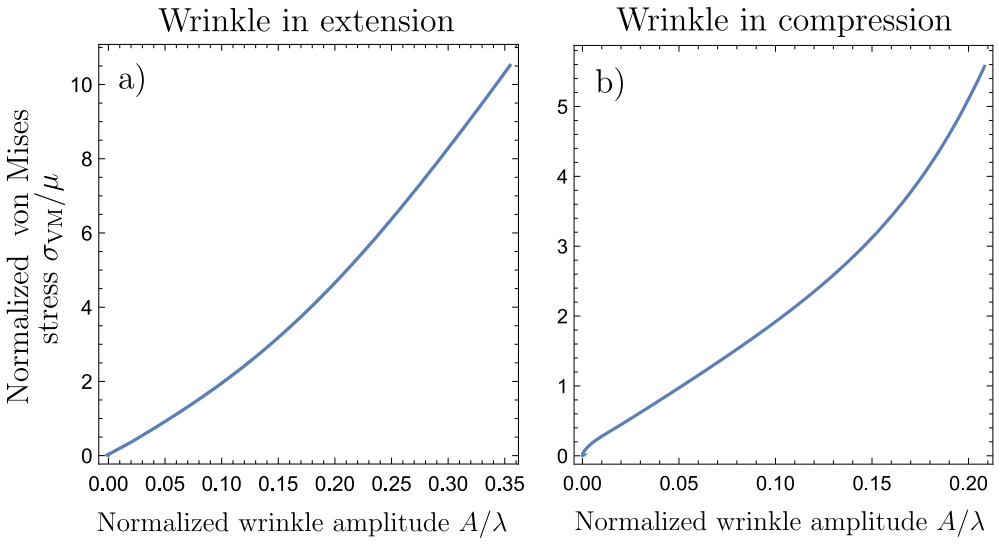

Fig. A.9. The diagrams show the normalized von Mises stress as a function of the normalized wrinkle amplitude for the location of (a) maximum extension of the substrate and (b) maximum compression in the substrate, which deforms as a consequence of the compressed film, that is attached at the surface of the substrate. The results are taken from Abaqus simulation presented in Fig. 5(c). The location of the maximum extension/compression of the substrate is on the substrate–film interface, right at the top/bottom of a wrinkle. As shown panels (a) and (b) the neo-Hookean material exhibits effective stiffening although the neo-Hookean material behaves as effectively softening in a uni-axial extension.

A.4. Effectively stiffening effects in wrinkling on neo-Hookean substrate

Although the neo-Hookean material model exhibits an effective softening stress–strain characteristic during a uni-axial extension, the stress–strain characteristic during a plane strain film–substrate setting, where the film stretches the substrate, is effectively stiffening. This is shown in Fig. A.9(a) and (b) where the normalized von Misses stress is plotted as a function of the normalized wrinkle amplitude for the deformation pattern, shown in Fig. 5(c), which is obtained from the same Abaqus simulation. The location of the maximum extension/compression of the substrate is on the substrate–film interface, right at the top/bottom of a wrinkle.

References

Allen, H.G., 1969. Analysis and Design of Structural Sandwich Panels. Pergamon, New York.

Antman, S.S., 1973. The theory of rods. In: Truesdell, C. (Ed.), Linear Theories of Elasticity and Thermoelasticity Linear and Nonlinear Theories of Rods, Plates, and Shells. Springer Berlin Heidelberg, Berlin, Heidelberg, pp. 641–703.

Attenburrow, G., Goodband, R., Taylor, L., Lillford, P., 1989. Structure, mechanics and texture of a food sponge. J. Cereal Sci. 9 (1), 61–IN1. http://dx.doi.org/10.1016/S0733-5210(89)80024-4, URL https://www.sciencedirect.com/science/article/pii/S0733521089800244.

Audoly, B., 2011. Localized buckling of a floating Elastica. Phys. Rev. E 84 (1), 011605.

Audoly, B., Boudaoud, A., 2008. Buckling of a stiff film bound to a compliant substrate—Part I:: Formulation, linear stability of cylindrical patterns, secondary bifurcations. J. Mech. Phys. Solids 56 (7), 2401–2421. http://dx.doi.org/10.1016/j.jmps.2008.03.003.

Balbi, V., Kuhl, E., Ciarletta, P., 2015. Morphoelastic control of gastro-intestinal organogenesis: Theoretical predictions and numerical insights. J. Mech. Phys. Solids 78, http://dx.doi.org/10.1016/j.jmps.2015.02.016.

Ben Amar, M., Goriely, A., 2005. Growth and instability in elastic tissues. J. Mech. Phys. Solids 53, 2284–2319. http://dx.doi.org/10.1016/j.jmps.2005.04.008.

Brau, F., Vandeparre, H., Sabbah, A., Poulard, C., Boudaoud, A., Damman, P., 2011. Multiple-length-scale elastic instability mimics parametric resonance of nonlinear oscillators. Nat. Phys. 7 (1), 56–60. http://dx.doi.org/10.1038/nphys1806.

Brojan, M., Terwagne, D., Lagrange, R., Reis, P.M., 2015. Wrinkling crystallography on spherical surfaces. Proc. Natl. Acad. Sci. 112 (1), 14–19. http://dx.doi.org/10.1073/pnas.1411559112, arXiv:https://www.pnas.org/doi/pdf/10.1073/pnas.1411559112 URL https://www.pnas.org/doi/abs/10.1073/pnas.1411559112.

Cao, Y., Hutchinson, J.W., 2012. From wrinkles to creases in elastomers: the instability and imperfection-sensitivity of wrinkling. Proc. R. Soc. A 468 (2137), 94–115. http://dx.doi.org/10.1098/rspa.2011.0384, arXiv:https://royalsocietypublishing.org/doi/pdf/10.1098/rspa.2011.0384 URL https://royalsocietypublishing.org/doi/abs/10.1098/rspa.2011.0384.

Chen, X., Hutchinson, J.W., 2004. Herringbone buckling patterns of compressed thin films on compliant substrates. J. Appl. Mech. 71 (5), 597–603. http://dx.doi.org/10.1115/1.1756141, arXiv:https://asmedigitalcollection.asme.org/appliedmechanics/article-pdf/71/5/597/5471575/597_1.pdf.

Fosdick, R.L., Schuler, K.W., 1969. On Ericksen's problem for plane deformations with uniform transverse stretch. Internat. J. Engrg. Sci. 7 (2), 217–233. http://dx.doi.org/10.1016/0020-7225(69)90058-5, URL https://www.sciencedirect.com/science/article/pii/0020722569900585.

Hosseinpour, A., Katbab, A.A., Ohadi, A., 2022. Improving the sound absorption of a highly deformable nanocomposite foam based on ethylene-propylene-diene-monomer (EPDM) infused with multi-walled carbon nanotubes (MWCNTs) to absorb low-frequency waves. Eur. Polym. J. 178, 111522. http://dx.doi.org/10.1016/j.eurpolymj.2022.111522, URL https://www.sciencedirect.com/science/article/pii/S0014305722005262.

Huang, Z., Hong, W., Suo, Z., 2005. Nonlinear analyses of wrinkles in a film bonded to a compliant substrate. J. Mech. Phys. Solids 53 (9), 2101–2118. http://dx.doi.org/10.1016/j.jmps.2005.03.007, URL https://www.sciencedirect.com/science/article/pii/S0022509605000700.

Huck, W.T.S., 2005. Hierarchical wrinkling. Nature Mater. 4 (4), 271–272. http://dx.doi.org/10.1038/nmat1356.

Hunt, G.W., Bolt, H.M., Thompson, J.M.T., 1989. Structural localization phenomena and the dynamical phase-space analogy. Proc. R. Soc. A 425 (1869), 245–267. http://dx.doi.org/10.1098/rspa.1989.0105, arXiv:https://royalsocietypublishing.org/doi/pdf/10.1098/rspa.1989.0105 URL https://royalsocietypublishing.org/doi/abs/10.1098/rspa.1989.0105.

Hutchinson, J.W., 2016. Buckling of spherical shells revisited. Proc. R. Soc. A 472 (2195), 20160577. http://dx.doi.org/10.1098/rspa.2016.0577, arXiv:https://royalsocietypublishing.org/doi/pdf/10.1098/rspa.2016.0577 URL https://royalsocietypublishing.org/doi/abs/10.1098/rspa.2016.0577.

Hutchinson, J.W., Thompson, J.M.T., 2018. Imperfections and energy barriers in shell buckling. Int. J. Solids Struct. 148–149, 157–168. http://dx.doi.org/10.1016/j.ijsolstr.2018.01.030, URL https://www.sciencedirect.com/science/article/pii/S0020768318300325, Special Issue Dedicated to the Memory of George Simitses.

Kusuma Chandrashekhara, S., Zupan, D., 2024. Analyzing material softening and strain localisation through embedded strong discontinuity approach within velocity-based beam formulation. http://dx.doi.org/10.2139/ssrn.4687917.

Lavrenčič, M., Brank, B., Brojan, M., 2020. Multiple wrinkling mode transitions in axially compressed cylindrical shell-substrate in dynamics. Thin-Walled Struct. 150, 106700. http://dx.doi.org/10.1016/j.tws.2020.106700, URL https://www.sciencedirect.com/science/article/pii/S0263823119319391.

Li, B., Cao, Y.-P., Feng, X.-Q., Gao, H., 2012. Mechanics of morphological instabilities and surface wrinkling in soft materials: a review. Soft Matter 8, 5728–5745. http://dx.doi.org/10.1039/C2SM00011C.

Li, B., Jia, F., Cao, Y.-P., Feng, X.-Q., Gao, H., 2011. Surface wrinkling patterns on a core-shell soft sphere. Phys. Rev. Lett. 106, 234301. http://dx.doi.org/10.1103/PhysRevLett.106.234301, URL https://link.aps.org/doi/10.1103/PhysRevLett.106.234301.

Liang, J., Huang, R., Yin, H., Sturm, J., Hobart, K., Suo, Z., 2002. Relaxation of compressed elastic islands on a viscous layer. Acta Mater. 50 (11), 2933–2944. http://dx.doi.org/10.1016/S1359-6454(02)00120-9, URL https://www.sciencedirect.com/science/article/pii/S1359645402001209.

Lifshitz, E., Kosevich, A., Pitaevskii, L., 1986. Chapter II - The equilibrium of rods and plates. In: Lifshitz, E., Kosevich, A., Pitaevskii, L. (Eds.), Theory of Elasticity (Third Edition), third ed. Butterworth-Heinemann, Oxford, pp. 38–86. http://dx.doi.org/10.1016/B978-0-08-057069-3.50009-7, URL https://www.sciencedirect.com/science/article/pii/B9780080570693500097.

Matoz-Fernandez, D.A., Davidson, F.A., Stanley-Wall, N.R., Sknepnek, R., 2020. Wrinkle patterns in active viscoelastic thin sheets. Phys. Rev. Res. 2, 013165. http://dx.doi.org/10.1103/PhysRevResearch.2.013165, URL https://link.aps.org/doi/10.1103/PhysRevResearch.2.013165.

McCormick, G.P., 1976. Computability of global solutions to factorable nonconvex programs: Part I — Convex underestimating problems. Math. Program. 10 (1), 147–175. http://dx.doi.org/10.1007/BF01580665.

Nikravesh, S., Ryu, D., Shen, Y.-L., 2020. Instabilities of thin films on a compliant substrate: Direct numerical simulations from surface wrinkling to global buckling. Sci. Rep. 10 (1), 5728. http://dx.doi.org/10.1038/s41598-020-62600-z.

Paulose, J., Nelson, D.R., 2012. Buckling pathways in spherical shells with soft spots. Soft Matter 9, 8227–8245, URL https://api.semanticscholar.org/CorpusID:85523143.

Sabbah, A., Youssef, A., Damman, P., 2016. Superhydrophobic surfaces created by elastic instability of PDMS. Appl. Sci. 6 (5), 1–8. http://dx.doi.org/10.3390/app6050152.

Smith, M., 2009. ABAQUS/Standard User's Manual, Version 6.9. Dassault Systèmes Simulia Corp, United States.

Stoop, N., Lagrange, R., Terwagne, D., Reis, P.M., Dunkel, J., 2015. Curvature-induced symmetry breaking determines elastic surface patterns. Nature Mater. 14 (3), 337–342. http://dx.doi.org/10.1038/nmat4202.

Tawarmalani, M., Sahinidis, N.V., 2002. Convexification and Global Optimization in Continuous And. Kluwer Academic Publishers, USA.

Terwagne, D., Brojan, M., Reis, P.M., 2014. Smart morphable surfaces for aerodynamic drag control. Adv. Mater. 26 (38), 6608–6611.

Thompson, J., Virgin, L., 1988. Spatial chaos and localization phenomena in nonlinear elasticity. Phys. Lett. A 126 (8), 491–496. http://dx.doi.org/10.1016/0375-9601(88)90045-X, URL https://www.sciencedirect.com/science/article/pii/037596018890045X.

Tuy, H., Van Thuong, N., 1988. On the global minimization of a convex function under general nonconvex constraints. Appl. Math. Optim. 18 (1), 119–142. http://dx.doi.org/10.1007/BF01443618.

Veldin, T., Brank, B., Brojan, M., 2019. Computational finite element model for surface wrinkling of shells on soft substrates. Commun. Nonlinear Sci. Numer. Simul. 78, 104863. http://dx.doi.org/10.1016/j.cnsns.2019.104863, URL https://www.sciencedirect.com/science/article/pii/S1007570419301832.

Veldin, T., Brank, B., Brojan, M., 2021. Discrete Kirchhoff–Love shell quadrilateral finite element designed from cubic Hermite edge curves and coons surface patch. Thin-Walled Struct. 168, 108268. http://dx.doi.org/10.1016/j.tws.2021.108268, URL https://www.sciencedirect.com/science/article/pii/S0263823121004894.

Veldin, T., Lavrenčič, M., Brank, B., Brojan, M., 2020. A comparison of computational models for wrinkling of pressurized shell-core systems. Int. J. Non-Linear Mech. 127, 103611. http://dx.doi.org/10.1016/j.ijnonlinmec.2020.103611, URL https://www.sciencedirect.com/science/article/pii/S0020746220302730.

Vliegenthart, G.A., Gompper, G., 2011. Compression, crumpling and collapse of spherical shells and capsules. New J. Phys. 13 (4), 045020. http://dx.doi.org/10.1088/1367-2630/13/4/045020.

Wadee, M.K., Hunt, G.W., Whiting, A.I.M., 1997. Asymptotic and Rayleigh–Ritz routes to localized buckling solutions in an elastic instability problem. Proc. R. Soc. Lond. Ser. A Math. Phys. Eng. Sci. 453 (1965), 2085–2107. http://dx.doi.org/10.1098/rspa.1997.0112, arXiv:https://royalsocietypublishing.org/doi/pdf/10.1098/rspa.1997.0112 URL https://royalsocietypublishing.org/doi/abs/10.1098/rspa.1997.0112.

Wang, Y., Du, Y., Xu, F., 2023. Strain stiffening retards growth instability in residually stressed biological tissues. J. Mech. Phys. Solids 178, 105360. http://dx.doi.org/10.1016/j.jmps.2023.105360, URL https://www.sciencedirect.com/science/article/pii/S0022509623001643.

Zavodnik, J., Košmrlj, A., Brojan, M., 2023. Rate-dependent evolution of wrinkling films due to growth on semi-infinite planar viscoelastic substrates. J. Mech. Phys. Solids 173, 105219. http://dx.doi.org/10.1016/j.jmps.2023.105219, URL https://www.sciencedirect.com/science/article/pii/S0022509623000236.